Monthly Notices
of the
ROYAL ASTRONOMICAL SOCIETY

MNRAS **469,** 3946–3964 (2017)
Advance Access publication 2017 May 6

doi:10.1093/mnras/stx1079

Lens modelling Abell 370: crowning the final frontier field with MUSE

David J. Lagattuta,[1]★ Johan Richard,[1] Benjamin Clément,[1] Guillaume Mahler,[1] Vera Patrício,[1] Roser Pelló,[2] Geneviève Soucail,[2] Kasper B. Schmidt,[3] Lutz Wisotzki,[3] Johany Martinez[1] and David Bina[2]

[1]*Univ Lyon, Univ Lyon1, Ens de Lyon, CNRS, Centre de Recherche Astrophysique de Lyon UMR5574, F-69230 Saint-Genis-Laval, France*
[2]*IRAP (Institut de Recherche en Astrophysique et Planétologie), Université de Toulouse, CNRS, UPS, F-31400 Toulouse, France*
[3]*Leibniz-Institut für Astrophysik Potsdam (AIP), An der Sternwarte 16, D-14482 Potsdam, Germany*

Accepted 2017 May 3. Received 2017 May 2; in original form 2016 November 6

ABSTRACT

We present a strong lensing analysis on the massive cluster Abell 370 (A370; $z = 0.375$), using a combination of deep multiband *Hubble Space Telescope* (*HST*) imaging and Multi-Unit Spectroscopic Explorer (MUSE) spectroscopy. From only 2 h of the MUSE data, we are able to measure 120 redshifts in the southern BCG area, including several multiply imaged lens systems. In total, we increase the number of multiply imaged systems with a secure redshift from 4 to 15, nine of which are newly discovered. Of these, eight are located at $z > 3$, greatly extending the redshift range of spectroscopically confirmed systems over previous work. Using these systems as constraints, we update a parametric lens model of A370, probing the mass distribution from cluster to galaxy scales. Overall, we find that a model with only two cluster-scale dark matter haloes (one for each BCG) does a poor job of fitting these new image constraints. Instead, two additional mass clumps – a central 'bar' of mass located between the BCGs, and another clump located within a 'crown' of galaxies in the northern part of the cluster field – provide significant improvements to the fit. Additional physical evidence suggests these clumps are indeed real features of the system, but with relatively few image constraints in the crown region, this claim is difficult to evaluate from a modelling perspective. Additional MUSE observations of A370 covering the entire strong-lensing region will greatly help these efforts, further improving our understanding of this intriguing cluster.

Key words: gravitational lensing: strong – techniques: imaging spectroscopy – galaxies: clusters: individual: Abell 370 – galaxies: high-redshift – dark matter.

1 INTRODUCTION

Galaxy clusters acting as strong gravitational lenses are powerful astrophysical laboratories. The lensed background sources constrain the cluster mass model, providing insight into the mass environments of the densest regions of the Universe (Bradač et al. 2008a,b; Hsu, Ebeling & Richard 2013; Massey et al. 2015). At the same time, the cluster magnifies these sources, making them larger, brighter and better resolved. This allows for more detailed studies of faint, low-mass, high-redshift galaxies, opening a window into the early Universe (Ebeling et al. 2009; Sharon et al. 2012; Monna et al. 2014; Patrício et al. 2016). Over the past decade, cluster lensing science has significantly expanded, and hundreds of new lensed systems have been discovered (e.g. Zitrin et al. 2011; Jauzac et al. 2014, 2015; Hoag et al. 2016; Kawamata et al. 2016). This is largely thanks to improved modelling techniques (such as Jullo et al. 2007 and Oguri 2010) and the efforts of deep, high-resolution imaging campaigns (e.g. Postman et al. 2012; Schmidt et al. 2014; Lotz et al. 2017), driven primarily by the *Hubble Space Telescope* (*HST*).

But while these imaging campaigns are able to identify and resolve background sources like never before, imaging alone does not provide high-precision ($\Delta z < 0.01$) redshift information, a crucial component in interpreting models and deriving their physical values. While some spectroscopic campaigns are underway (e.g. Rosati et al. 2014; Treu et al. 2015), acquiring spectra of lensed systems has, to date, largely been a long, costly and inefficient process. With the advent of Integral Field Unit (IFU) spectroscopy, however, this situation is rapidly changing. Leading the way in these efforts is the Multi-Unit Spectroscopic Explorer (MUSE; Bacon et al. 2010) a wide-field IFU on the Very Large Telescope (VLT) in Chile. With a large 1 arcmin^2 field of view and high sensitivity between 4800 and 9300 Å, MUSE is an incredibly efficient redshift engine, providing several hundred redshifts between $z = 0$ and $z = 6$ in only

★ E-mail: david-james.lagattuta@univ-lyon1.fr

a few hours of exposure time (e.g. Bacon et al. 2015). As an IFU, MUSE is also well suited for blind redshift surveys, able to detect emission lines from continuum-free sources without pre-selecting a redshift range. These objects (which are often missed in traditional broad-band imaging campaigns) include high-redshift, lensed Lyman α emitters. This has been, unsurprisingly, a boon to the lensing community, and some studies have already begun to take advantage of the MUSE data (e.g. Karman et al. 2015; Richard et al. 2015; Bina et al. 2016; Jauzac et al. 2016; Caminha et al. 2017).

In this work, we present new MUSE data of the strong lensing cluster Abell 370 (A370; Abell 1958). A370 is a massive cluster ($M_{\rm vir} = 2.3 \times 10^{15}\,{\rm M}_{\odot}$; Umetsu et al. 2011) at redshift $z = 0.375$ (Mellier et al. 1988) with historical significance to lensing: it contains one of the first known 'Giant Luminous Arc' features (Lynds & Petrosian 1986), which later became the first spectroscopically confirmed giant-arc lens system (Soucail et al. 1987, 1988; Lynds & Petrosian 1989). Thanks to this discovery, and the identification of other lensed features (Hammer 1987; Paczynski 1987; Fort et al. 1988; Mellier et al. 1991; Kneib et al. 1993), A370 became an important benchmark in the early days of lens modelling (e.g. Hammer 1991; Kneib et al. 1993; Smail et al. 1996; Bézecourt et al. 1999a,b). However, after an initial period of activity, interest in A370 slowly waned; there was little spectroscopic follow-up on the cluster, and it was not selected to be a part of massive cluster surveys such as MACS (Ebeling, Edge & Henry 2001) or CLASH (Postman et al. 2012), in spite of its high X-ray luminosity ($L_x = 1.1 \times 10^{45}$ erg s^{-1}; Morandi, Ettori & Moscardini 2007).

In 2010, a newly refurbished *HST* observed A370 to test its deep-imaging capabilities, generating renewed interest. This led to a new lens model (Richard et al. 2010), additional weak-lensing analyses (Medezinski et al. 2011; Umetsu et al. 2011) and its eventual selection as one of the Hubble Frontier Fields (HFF) clusters (Lotz et al. 2017). Several groups have since modelled the cluster (see the HFF archive[1] and also Richard et al. 2014 and Johnson et al. 2014), but (until recently) only three lensed systems have had a secure redshift, all with $z < 1.2$ (see Section 3.1.1 for details). As a result, these models are only able to probe the critical line region of the cluster out to small radii. While recent work by Diego et al. (2016) has increased the number of secure-redshift systems, the highest of these is still $z < 2$. Here, we extend the redshift range of spectroscopically confirmed systems even further and present newly discovered systems as well. By combining the MUSE spectroscopy with the current HFF data, we can therefore improve on existing lens models, probing the mass distribution out to larger scales and with much higher precision. In this way, we can improve our view of this massive cluster in conjunction with the final HFF data release.

Overall, this work is organized as follows: in Section 2, we describe the MUSE and HFF data and the data reduction processes we used. In Section 3, we describe how we extract MUSE redshifts and present the A370 redshift catalogue, paying particular attention to redshifts of the multiply imaged galaxies. Using these redshifts, we construct a new mass model, which we present in Section 4. We discuss the results of the mass modelling and make predictions for future work in Section 5. Finally, we briefly conclude in Section 6. Throughout this paper, we assume a standard cosmological model with $\Omega_M = 0.3$, $\Omega_\Lambda = 0.7$ and $H_0 = 70$ km s^{-1} Mpc^{-1}. Using this model, 1 arcsec covers a physical distance of 5.162 kpc at the A370 redshift ($z = 0.375$). All magnitudes are measured using the AB system.

[1] https://archive.stsci.edu/pub/hlsp/frontier/abell370/models/

2 DATA

Lensing is a three-dimensional effect, sensitive to both the transverse and line-of-sight distances between objects. Therefore, we need a combination of imaging data (to identify lensed objects and measure their apparent positions) and redshift data (to measure radial distances) to construct an accurate lens model of A370.

2.1 *HST* imaging

HST imaging data of A370 were taken as part of the HFF Programme, and are publicly available on the HFF website.[2] While the imaging campaign for A370 is now complete, the Epoch 1 (v1.0) mosaics that we use in this work consist of deep Advanced Camera for Surveys (ACS; Ford et al. 2003) data in three optical bands, *F*435*W*, *F*606*W* and *F*814*W* (ID: 13504, PI: J. Lotz). These are supplemented by shallower *F*814*W* imaging from archival programmes: (ID: 11507, PI: K. Noll) and (ID: 11591, PI: J.-P. Kneib). Additionally, shallow, archival, Wide-Field Camera 3 (Kimble et al. 2008) data are available in three bands: *F*105*W* (ID: 13459, PI: T. Treu), *F*140*W* (ID: 11108, PI: E. Hu; ID: 13459, PI: T. Treu) and *F*160*W* (ID: 11591, PI: J.-P. Kneib; ID: 14216, PI: R. Kirshner), and a shallow, pilot HF exposure, also in the *F*140*W* band.

Individual exposures are reduced and stacked by the HFF team directly, using the standard Pyraf/STSDAS pipeline. Additionally, the ACS mosaics are further corrected with a 'self-calibration' technique to eliminate charge transfer inefficiency effects and low-level pixel noise[3] (J. Anderson, in preparation). The full reduction procedure is described in the A370 HFF data archive.[4]

After combining all exposures, total integration times are 51 400, 25 316, 130 643, 2335, 12 894 and 9647 s for the *F*435*W*, *F*606*W*, *F*814*W*, *F*105*W*, *F*140*W* and *F*160*W* bands, respectively. This is equivalent to 20, 10, 52, 1, 5 and 4 *HST* orbits. Collectively, this represents one of the deepest, highest resolution imaging of A370 ever taken, and corresponds to average limiting magnitudes of 29.3 in the optical bands and 27.6 in the near-IR bands. A colour image of the cluster field consisting of the *F*435*W*, *F*606*W* and *F*814*W* mosaics is shown in Fig. 1.

2.2 MUSE spectroscopy

MUSE observations of A370 were taken on UT 2014 November 20, as part of the Guaranteed Time Observing (GTO) Programme 094.A-0115(A) (PI: Richard). In total, we observed four 30-min exposures in WFM-NOAO-N mode, centred at ($\alpha = 2^{\rm h}\,39^{\rm m}\,53\overset{\rm s}{.}111$, $\delta = -1^\circ\,34'\,55\overset{''}{.}77$). We applied a small ($\sim 0.5$ arcsec) dither pattern between exposures to average out systematics on the detector, and we alternated taking exposures between PA $= 0^\circ$ and PA $= 8^\circ$ to reduce the systematic striping pattern caused by the IFU image slicers. The full observational footprint can be seen in Fig. 1. Typical field of view during the observations was 0.75 arcsec, as measured by stars in the field.

The raw data were reduced through the MUSE pipeline (Weilbacher et al. 2012, 2014) provided by ESO (version 1.2). This pipeline performs all basic reduction techniques: bias and flat-field correction (using a combination of internal flats and illumination and twilight exposures), wavelength and geometric calibration, sky

[2] http://www.stsci.edu/hst/campaigns/frontier-fields/
[3] http://www.stsci.edu/hst/acs/software/Selfcal
[4] https://archive.stsci.edu/pub/hlsp/frontier/abell370/images/hst/v1.0-epoch1/hlsp_frontier_hst_acs-00_abell370_v1.0-epoch1_readme.pdf

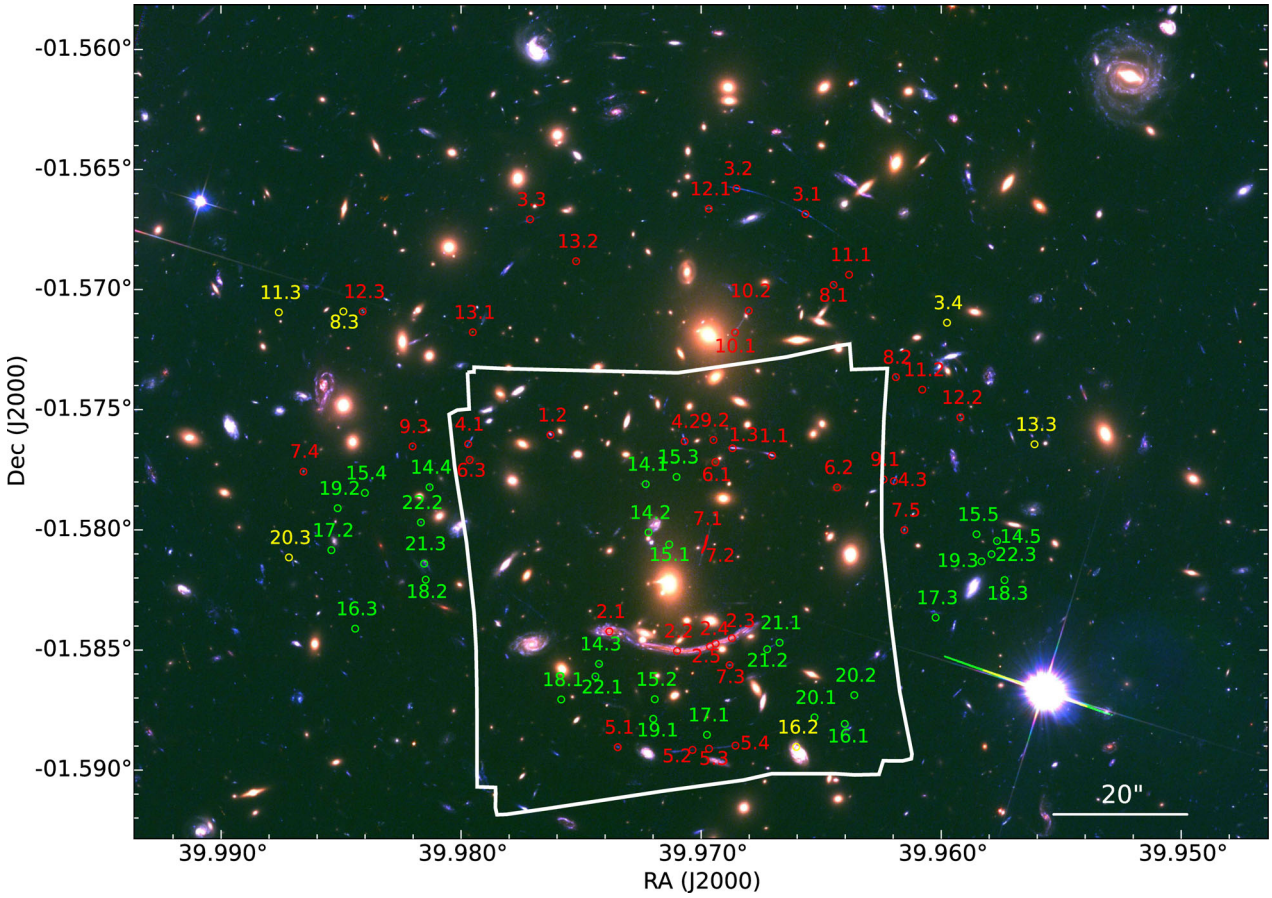

Figure 1. A colour image of the A370 field of view, using the *F*435*W*, *F*606*W* and *F*814*W* observations from the HFF project. The region of the cluster covered by the MUSE GTO programme is shown in white. In addition, the positions of the multiply imaged systems used as constraints in the mass model (Section 4) are shown as coloured circles. Previously known systems are in red, while newly identified objects are in green. Images predicted by the model but not detected in either imaging or spectroscopic data are shown in yellow.

subtraction, flux calibration and telluric correction. The A370 data were flux-calibrated using a combination of several standard stars observed under photometric conditions. After basic corrections, we align individual exposures to a common world coordinate system (WCS) with SCAMP (Bertin 2006), shifting each frame relative to a reference image, which in this case is the *F*814*W* HFF data. We then transform the re-aligned images into data cubes, resampling all pixels on to a common three-dimensional grid with two spatial and one spectral axis. The final spectral resolution of the cubes varies from $R = 2000$ to $R = 4000$, with a spectral range between 4750 and 9350 Å. To ensure that cubes are properly Nyquist-sampled, we set the wavelength grid to 1.25 Å pixel^{-1}. The final spatial resolution is 0.2 arcsec pixel^{-1} in order to properly sample the PSF.

Next, we process each cube with the Zurich Atmosphere Purge (ZAP; Soto et al. 2016), a software package that uses a principal component analysis technique to remove known systematics from the sky model, further improving sky-subtraction residuals. To account for changes in sky transmittance from exposure to exposure, we compare the fluxes of stars common to each cube. The cube with the brightest flux values is taken as a new photometric standard, and we scale the zero-points of the other cubes until the fluxes agree across all exposures. We then merge all cubes together to create a combined master cube. During the merging process, we apply a 3σ clipping routine to reject outliers, eliminating cosmic ray strikes and hot pixels on the detector. As a final step, we re-run the ZAP process on the master cube in order to eliminate low-level sky residuals that can only be seen in the improved signal-to-noise ratio of the combined data.

3 REDSHIFT MEASUREMENT AND SPECTROSCOPIC CATALOGUE

After reducing the data, we probe the MUSE cube for redshifts using two complementary techniques: (1) an automated emission line detection program, and (2) a customized, interactive data visualization tool designed to extract MUSE aperture spectra by hand.

The automated program, MUSELET,[5] is included as part of the Muse Python Data Analysis Framework (MPDAF[6]) version 2.0. It first creates narrow-band images of the data, averaging the flux over a narrow emission wavelength range and then subtracting a local continuum. For the A370 cube, we choose an emission window of 6.25 Å (spanning five MUSE wavelength slices), with each window centred on one of the original wavelength planes. The continuum is created by averaging two 25 Å slices, immediately bluewards and redwards of the emission window. After creating the narrow-band images, MUSELET uses Source Extractor (Bertin & Arnouts 1996) to

[5] http://mpdaf.readthedocs.io/en/latest/muselet.html
[6] https://git-cral.univ-lyon1.fr/MUSE/mpdaf

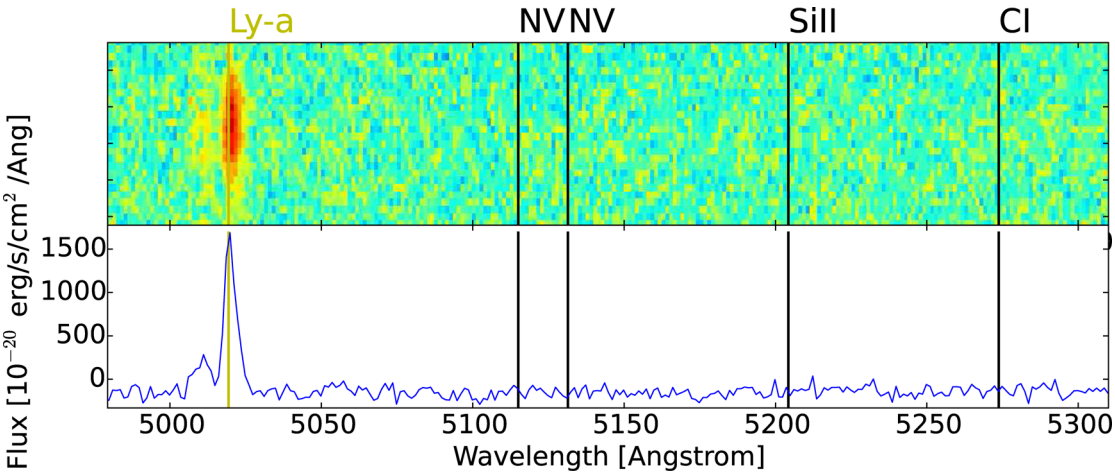

Figure 2. Sample spectrum extracted by our interactive Python tool. Here, we see Image 14.1, a newly detected Lyman α emitter at redshift $z = 3.1309$. The Lyman α emission is clearly detected in the spectrum and is double-peaked.

identify emission features in each image, then merges these features together into a final master catalogue. Emission features at different wavelengths are considered to belong to the same source if they fall within 0.8 arcsec of each other (i.e. within the seeing FWHM) in the case of continuum-free detections, or if they fall within half of the effective radius ($r_e/2$) of a continuum-emission object. For every source that has multiple emission lines identified, MUSELET fits a redshift using a template of known spectral lines. To ensure the accuracy of the MUSELET fit, we manually inspect the line features of each identified redshift before adding it to the final catalogue.

In cases where an obvious galaxy appears in the *HST* image or MUSE cube but is undetected (absorption galaxies) or unclassified (single emission-line galaxies) by MUSELET, we instead use the interactive tool. The tool, a custom-made PYTHON script, collapses the data cube along the wavelength axis, creating a 'white-light' image of the field. A second panel, matched to the WCS of the cube, shows a corresponding *HST* image to help identify the target galaxy. Once a galaxy has been identified, a user can draw a (circular or rectangular) aperture around the target object, which will extract both a 2D and 1D spectrum from the cube. From these spectra, the user can then interactively fit a redshift to the galaxy, using the same set of lines as the automatic line-finder. An example of this process can be seen in Fig. 2. As an additional check, we run the redshift-measuring software AUTOZ (Baldry et al. 2014) on the extracted 1D spectrum. In all cases, we find the difference between the manual and AUTOZ fits to be less than $\delta z = 0.001$.

After running both methods on the A370 cube, we combine all of the redshift results into a final catalogue. Overall, we securely identify 120 redshifts, consisting of multiply imaged systems, cluster members, foreground interlopers, background sources and stars. The spatial and spectral distributions of these redshifts are shown in Fig. 3.

3.1 Multiply imaged systems

Multiply imaged background sources are particularly important in this work, since they provide strong constraints on the lensing mass model (see Section 4). Using a combination of the HFF imaging and the MUSE spectroscopy, we are able to identify and confirm the redshifts of previously known multi-image systems and identify new systems as well.

3.1.1 Previously known systems

Prior to the release of the newest HFF and MUSE data, 13 multi-image objects were identified in the A370 field (Richard et al. 2014) including three with known redshifts: Systems 1 (Kneib et al. 1993), 2 (Soucail et al. 1988) and 6 (Richard et al. 2014). A tentative guess for System 4 ($z = 1.275$) using the VLT/FORS2 grism spectroscopy was also presented in Richard et al. (2014). Of these systems, seven have at least one image that falls within the MUSE A370 footprint: Systems 1, 2, 4, 5, 6, 7 and 9. Using the MUSE data, we are able to confirm the previous redshifts of Systems 1 ($z = 0.8041$), 2 ($z = 0.7251$) and 6 ($z = 1.0633$), refine and secure the redshift for System 4 ($z = 1.2728$) and provide new redshifts for Systems 5 ($z = 1.2775$) and 7 ($z = 2.7512$). We note that these new redshifts are within 2σ of the values predicted in the Richard et al. (2014) lens model (System 4: $z = 1.34 \pm 0.03$; System 5: $z = 1.30 \pm 0.05$; System 7: $z = 4.97 \pm 1.17$), a reasonably good agreement. We are unable to identify any strong features in System 9 because it is too faint for a secure measurement. However, Diego et al. (2016) identify [O II] and [O III] features for the system in the *HST* grism spectroscopy, placing it at $z = 1.52$. We note that this redshift is consistent with a non-detection in MUSE, since it falls in the 'redshift desert' where no strong emission features appear in the MUSE wavelength range. Additionally, Diego et al. (2016) also identify faint [O III] emission for System 3 at $z = 1.95$. We adopt these redshift values in this work, also.

3.1.2 New systems

In addition to the known objects, we also identify nine new multiply imaged systems in the MUSE field (Systems 14–22). Diego et al. (2016) independently identify four of these systems: 14, 20, 21 and 22 (labelled Systems 10, 29, 26 and 18, respectively, in their work) though without spectroscopic redshifts. With the exception of System 21 (identified by [O II]), these new systems are all strong Lyman α emitters, located at considerably higher redshifts ($3 < z < 6$) than those previously identified. Systems 14 and 22 are particularly interesting, as they are reasonably close together and have an identical redshift ($z = 3.1309$). This suggests that they could be an interacting pair of galaxies, and indeed, narrow-band imaging shows that the emission-line regions of the two are clearly overlapping (Fig. 4). Careful observation of the HFF data reveals at

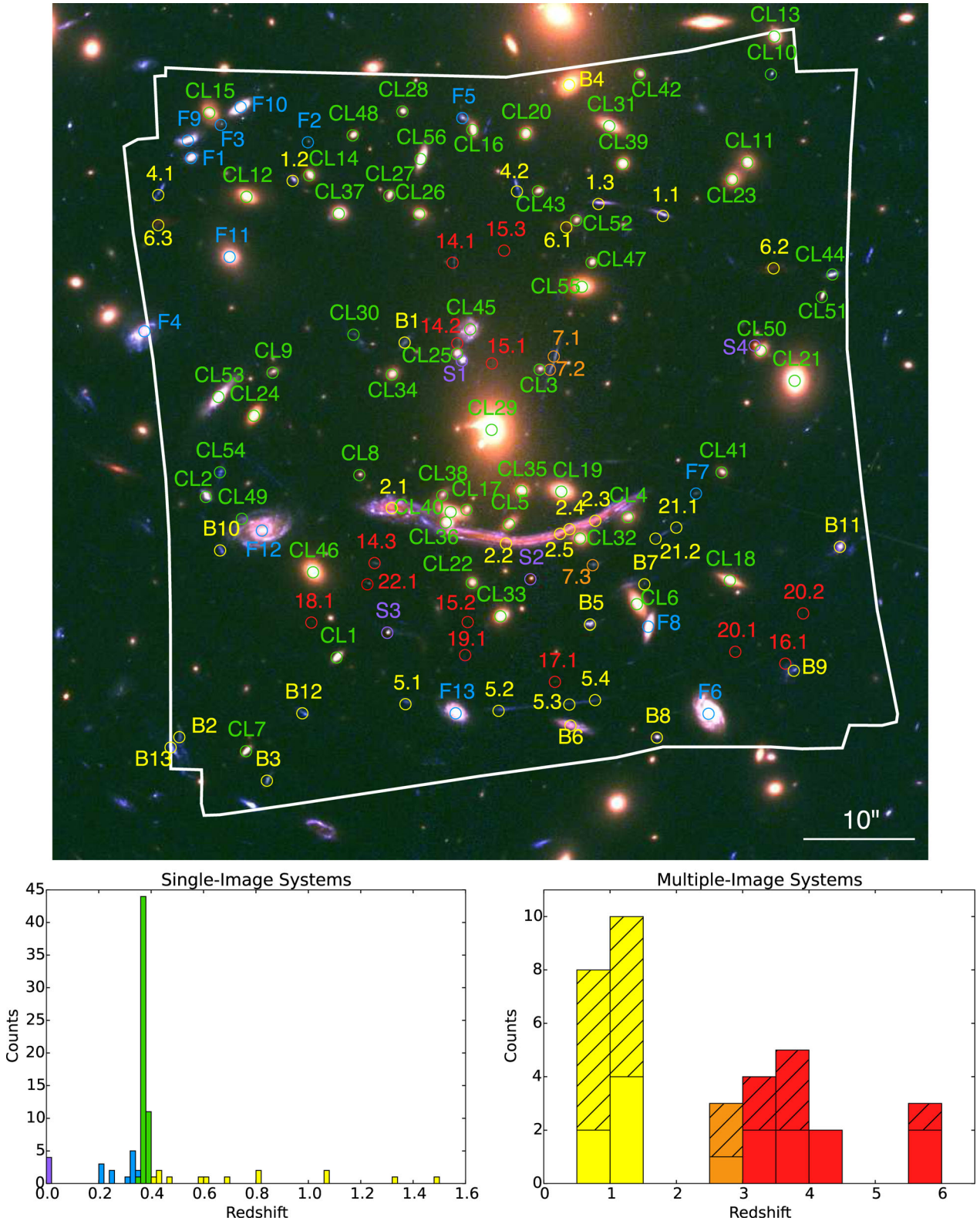

Figure 3. Top: positions of all objects with a secured redshift in the MUSE GTO cube. The colour of each circle represents the object's type and redshift range, according to the following scheme. Purple: star ($z = 0$), blue: foreground galaxy ($0 < z < 0.35$), green: cluster member ($0.35 \leq z \leq 0.4$), yellow: [O II] emitter ($0.4 < z < 1.5$), orange: [C III] emitter ($1.5 \leq z < 3.0$), red: Lyα emitter ($z \geq 3.0$). Object labels correspond to entries in Table 1 (multiply imaged systems), Table 2 (cluster members) and Table 3 (foreground and background objects). Bottom left: redshift distribution of all singly imaged systems in the cube. The colour scheme is the same as in the position map. A clear overdensity of galaxies can be seen at the cluster redshift range, as expected. Bottom right: similar redshift distribution, but for the multiply imaged systems. Solid colour lines represent individual systems, while the hashed lines represent all the counterimages that make up these systems.

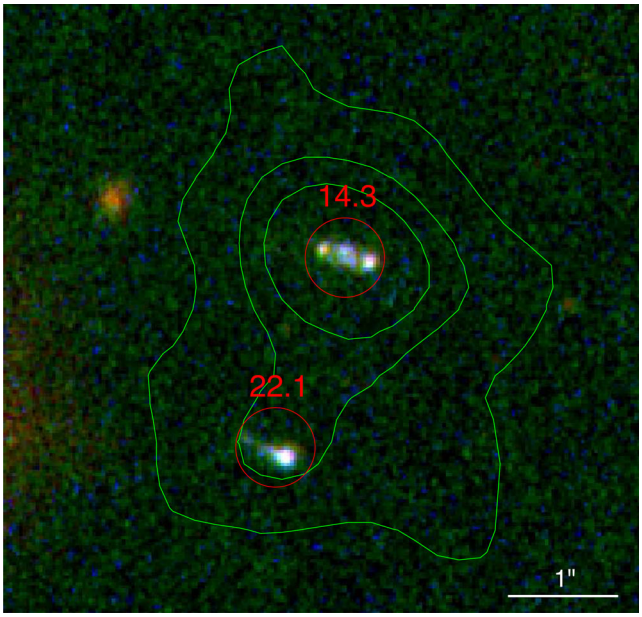

Figure 4. Close-up of the area containing Images 14.3 and 22.1, two newly identified, multiply imaged, Lyman α-emitting galaxies. While the *HST* imaging alone shows that the two galaxies are in close proximity to one another and have similar colours, new spectroscopy from MUSE reveals that they have exactly the same redshift ($z = 3.1309$). Additionally, narrow-band imaging of the emission line (green contours) shows that there is a significant overlap between the galaxies' Lyman α haloes, suggesting that the two galaxies could be interacting.

least some flux associated with each of the new systems in broad-band imaging, but in some cases – especially Systems 15 and 16 – this flux is extremely faint and contaminated by brighter objects nearby. Spectra of all systems in the MUSE field of view are shown in Fig. 5. The full list of multiply imaged systems, including all identified and/or model-predicted counterimages of a given system, is presented in Table 1.

3.2 Cluster members

Cluster members make up the largest subgroup in the spectroscopic catalogue, with 56 confirmed redshifts. To identify cluster members, we select all galaxies that fall between $z = 0.35$ and $z = 0.4$, a $\delta v = 15\,000$ km s^{-1} cut in velocity space centred on the A370 central redshift ($z = 0.375$). In the overall redshift catalogue, these boundaries naturally separate the cluster overdensity from all other objects, and a large fraction of galaxies in this range fall on both the (*F*435*W*–*F*606*W*) and (*F*606*W*–*F*814*W*) red sequences. While a majority of objects are passive, elliptical galaxies showing only absorption features, some do show strong [O II], [O III] and/or Hα emission. Of these emission-line galaxies, CL49 (located close to the bright, foreground spiral F12) is unique, as it is the only detected cluster member in the MUSE field of view without an *HST* counterpart (Fig. 6). Strangely, the object also appears to have a divergent velocity field: moving in either direction along the long axis, the flux becomes more and more redshifted relative to the centre. We do not have an explanation for this behaviour at this time, though it would be interesting to revisit in future work.

Cluster galaxy positions are represented by green circles in the top panel of Fig. 3. The redshifts themselves are presented in Table 2.

3.3 Other objects

In addition to cluster members and multiply imaged systems, the catalogue also contains a number of foreground objects and singly imaged background objects at various redshifts. We identify four stars within the MUSE field of view, mostly located near the BCG. Beyond the Milky Way, we find 13 galaxies in the foreground of the cluster, between $z = 0.2$ and $z = 0.35$. Nearly all of these objects are optically blue and have emission features, in particular a very strong Hα line. However, object F11 ($z = 0.3275$) shows strong absorption line features, with only weak [O II] emission. Behind the cluster, we find an additional 13 objects at redshifts between $z = 0.41$ and $z = 1.5$. Here again, these systems are largely identified by strong [O II] and/or [O III] emission lines, however object B4 ($z = 0.4655$) is another absorption-line galaxy showing weak [O II] emission. Information on all singly imaged objects can be found in Table 3.

4 LENS MODELLING

To measure the mass distribution of A370, we follow a procedure used in previous works (e.g. Johnson et al. 2014; Richard et al. 2014): namely, we model the system as a collection of mass clumps, including both large-scale dark matter haloes representing cluster potentials and smaller, galaxy-scale haloes representing individual galaxies. Each halo, regardless of size, is assumed to have a truncated dual Pseudo-Isothermal Elliptical mass distribution (dPIE; Elíasdóttir et al. 2007). The description of a dPIE halo consists of seven parameters: position (α and δ), velocity dispersion (σ_0), position angle (θ), ellipticity (ε) and two scale radii ($r_{\rm core}$ and $r_{\rm cut}$) that modify the halo's mass slope. Here, $r_{\rm core}$ represents the halo's inner core radius, inside of which the mass slope flattens instead of increasing isothermally. Finally, $r_{\rm cut}$ represents the halo's cut-off radius, outside of which the mass slope drops more steeply.

During the optimization process, we allow most cluster halo parameters to freely vary within a given prior distribution, but we fix $r_{\rm cut}$ to a large value of 800 kpc (155 arcsec). This is because the current data do not extend far enough to meaningfully constrain its value. To limit the overall size of the parameter space, we place additional restrictions on the galaxy-scale haloes, adopting a light-traces-mass approach that assumes correlation between the observed baryons and their galaxy haloes. Galaxy positions, ellipticities and position angles are fixed to values measured from the *F*814*W* HFF data, while $r_{\rm core}$, $r_{\rm cut}$ and σ_0 are scaled based on the galaxy's luminosity (L), relative to an L^* galaxy. At the A370 cluster redshift, $m^*_{\rm F814W} = 18.31$. We fix $r^*_{\rm core}$ to be 0.15 kpc, while we allow $r^*_{\rm cut}$ to vary with a uniform prior between 10 and 50 kpc. The $r^*_{\rm cut}$ value is kept low to account for tidal stripping effects by the cluster haloes (Halkola, Seitz & Pannella 2007; Limousin et al. 2007a; Natarajan et al. 2009). Similarly, we allow (σ^*_0) to vary, but we instead assume a Gaussian prior distribution with mean $\mu_{\rm pdf} = 158$ km s^{-1} and width $\sigma_{\rm pdf} = 27$ km s^{-1}, following the Bernardi et al. (2003) observations of early-type galaxies in high-density environments in the Sloan Digital Sky Survey.

Finally, we model three galaxy-scale haloes separately from the scaling relation: the two BCGs and another bright galaxy (GAL1) lying close to the System 2 giant arc. The southern BCG and GAL1 (objects Cl29 and Cl32, respectively, in Fig. 3) are close enough and massive enough to significantly affect the shape of System 2. The northern BCG mildly influences the orientation of the northern cluster potential. Like the other galaxy potentials, we fix the position, PA and ellipticity values to match the *F*814*W* HFF data. We also fix $r_{\rm core}$, though we assume different values (0.14 kpc for the

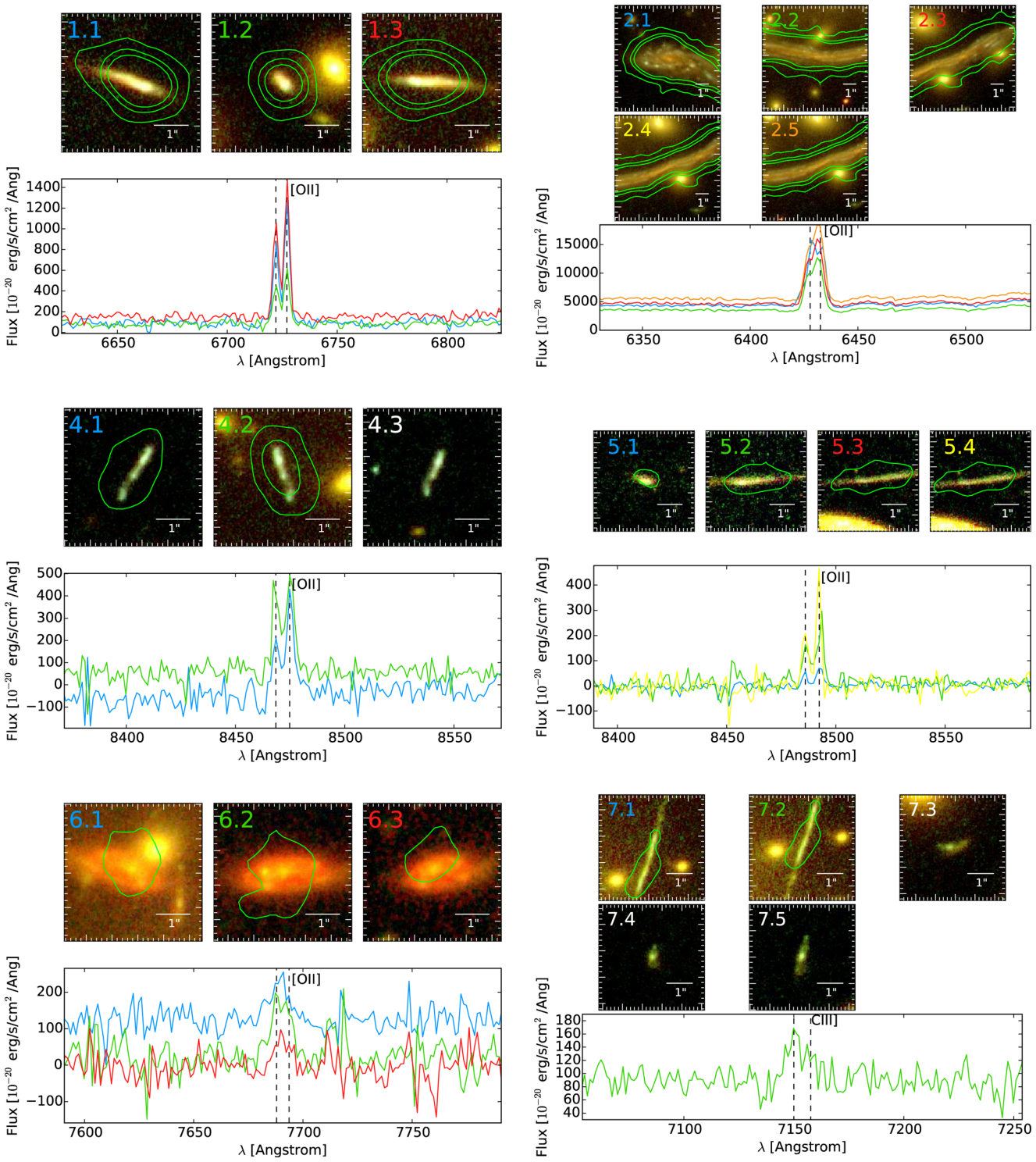

Figure 5. (a) Multiply imaged systems with MUSE spectroscopy. Individual members of a given system (constraints) are labelled according to Table 1. In the top panels, we show colour images of each constraint, using the *F*435*W*/*F*606*W*/*F*814*W* HFF bands for the RGB channels of the figure. The one exception is System 6, which instead uses a colour scheme of *F*435*W*/*F*814*W*/*F*160*W* to better highlight its morphology. Green contours represent the 1σ, 3σ and 5σ (per pixel) levels of the brightest emission line seen in narrow-band imaging of the MUSE data cube. Cutouts of the extracted spectra, again centred on the brightest emission line, are shown in the bottom panel. The label colour of a given constraint matches the colour of its corresponding spectrum. Constraints that fall outside of the MUSE field of view, and thus have no MUSE spectroscopy, are labelled in white. With the exception of System 16, which includes the undetected Image 16.2, only image constraints used in the A370 mass model are displayed here. Model predictions outside of the MUSE footprint where we find no obvious *HST* counterpart are not shown. For merging pairs of images (Images 5.3/5.4, 7.1/7.2 and 21.1/21.2) we use a common extraction region for both spectra. The combined spectrum of both images then appears as a single line in the plot. (b) New MUSE-identified systems. The contours seen in Image 14.3 are identical to those in Fig. 4, highlighting the overlap between the Lyman α haloes of Images 14.3 and 22.1. (c) The final three MUSE-identified systems. We again see the overlap between the Lyman α haloes of Images 14.3 and 22.1.

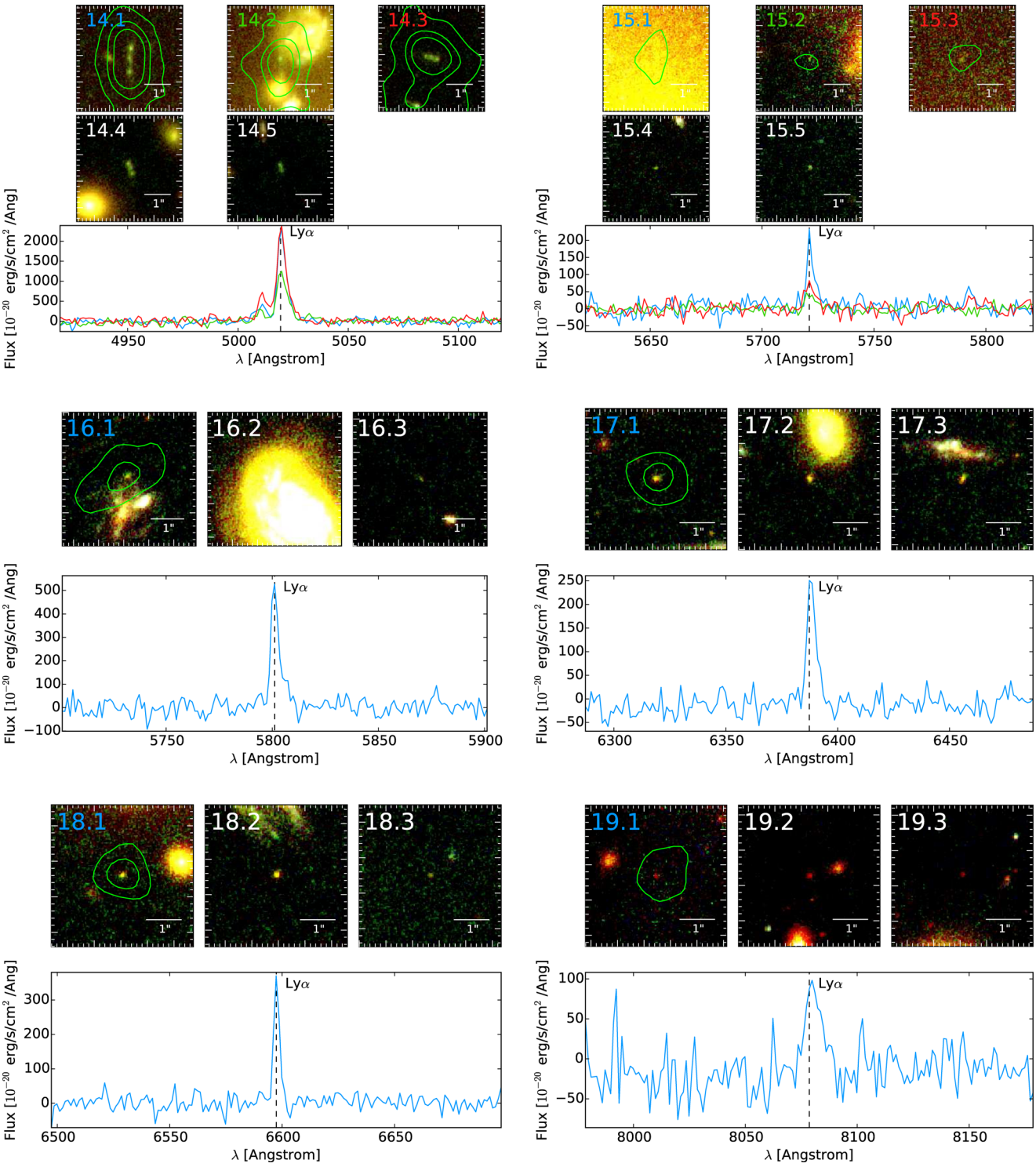

Figure 5 – *continued*

BCGs, 0.06 kpc for GAL1) based on their magnitudes, which are consistent with the original scaling relation. The values of σ_0 and $r_{\rm cut}$ are allowed to vary freely, using their magnitude-scaled values relative to L^* as a starting point.

Individual galaxies that we include in the model as cluster-member haloes are selected through a colour cut, using the three optical HFF bands. Additionally, we limit the selection to bright galaxies ($m_{\rm F814W} < 22.6$), since beyond this cutoff – roughly equivalent to $\sim$0.02 L_* – galaxies will have a negligible effect on the mass budget. We also exclude galaxies at distances beyond $R = 70$ arcsec from the cluster centre ($\alpha = 2^{\rm h}\,39^{\rm m}\,59\overset{\rm s}{.}9$, $\delta = -1^\circ\,34'\,36\overset{''}{.}5$), corresponding to $R > 360$ kpc in physical space, for similar reasons. For the colour cut itself, we construct the *F*435*W*–*F*606*W* and *F*606*W*–i814*W* colour–magnitude diagrams and look for evidence of a red sequence. The colour–magnitude diagrams are shown in the upper panels of Fig. 7, along with the boundary conditions

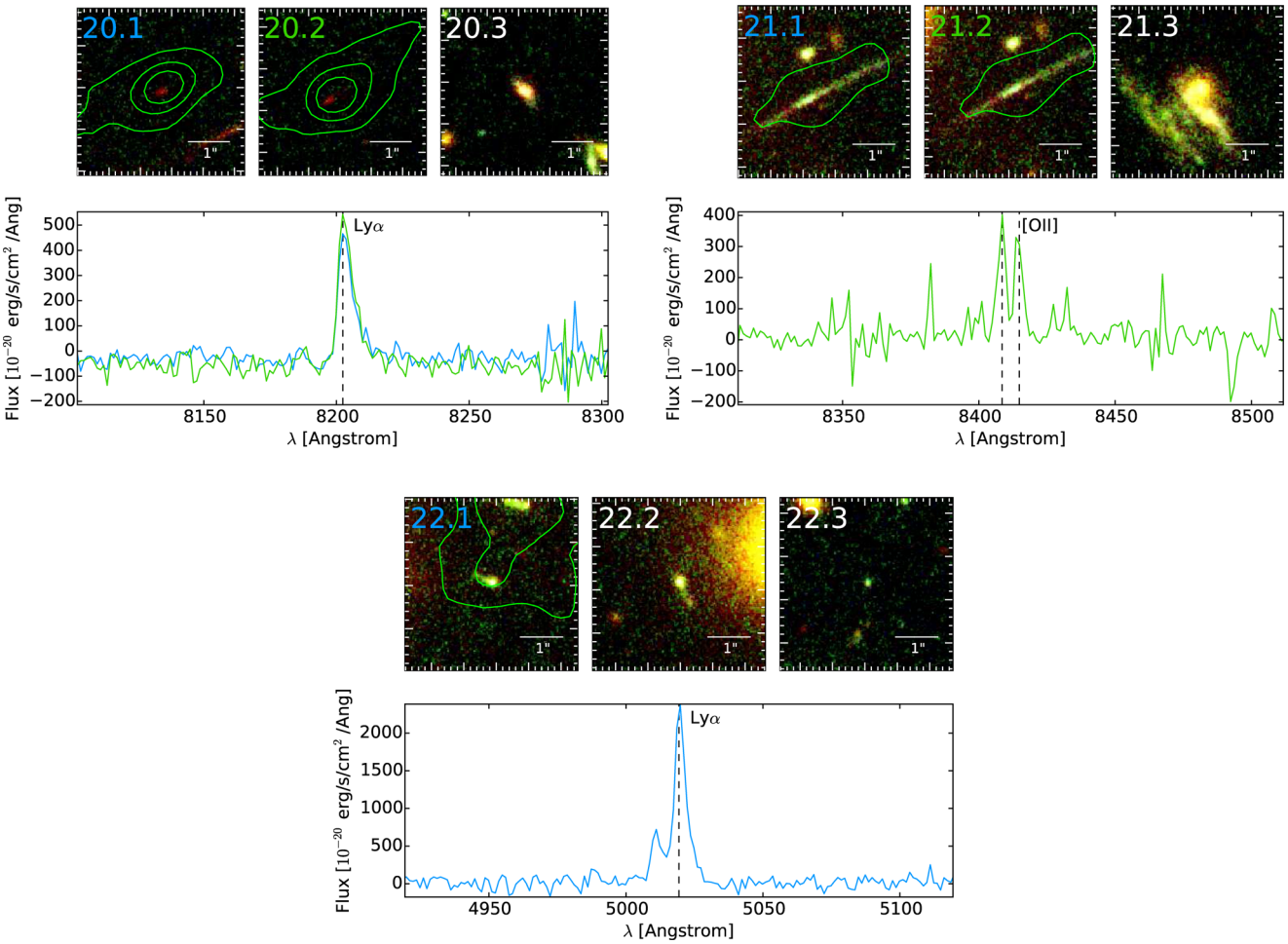

Figure 5 – *continued*

used to select candidate cluster members. These are given by

$$(-0.11 \times m_{\mathrm{F814W}}) + 4.06 \leq (m_{\mathrm{F435W}} - m_{\mathrm{F606W}})$$
$$(-0.11 \times m_{\mathrm{F814W}}) + 4.45 \geq (m_{\mathrm{F435W}} - m_{\mathrm{F606W}}) \quad (1)$$

for *F*435*W*–*F*606*W* and

$$(-0.04 \times m_{\mathrm{F814W}}) + 1.74 \leq (m_{\mathrm{F606W}} - m_{\mathrm{F814W}})$$
$$(-0.04 \times m_{\mathrm{F814W}}) + 1.93 \geq (m_{\mathrm{F606W}} - m_{\mathrm{F814W}}) \quad (2)$$

for *F*606*W*–*F*814*W*. We then combine the two plots into a colour–colour diagram and select galaxies that satisfy both red sequence cuts. The majority of these galaxies fall into a tight cluster locus (Fig. 7, bottom). To measure galaxy photometry, we run SExtractor (Bertin & Arnouts 1996) in dual-image mode, using the *F*814*W* band data as the detection template. In the region covered by the MUSE footprint, we further refine the selection process by including all spectroscopically confirmed cluster members (including the bluer, late-type galaxies missed by the colour–colour cut) and rejecting all non-cluster members regardless of their colours or magnitudes.

We constrain the mass model with the positions of known multiply imaged systems, however, we first revise the interpretation of System 5, previously described as a three-image system (5.1, 5.2, 5.3). Image 5.3 is actually located close to a background galaxy at $z = 0.6$ (object B6 in Table 3) that perturbs the lens model, and we add it as an additional galaxy-scale potential. As illustrated by a simulation of the lensing effect on Images 5.1 and 5.2, this small perturbation convincingly produces a merging pair of two additional images previously identified as 5.3 (Fig. 8). Therefore, we update our constraint list to include the new Image 5.3 and Image 5.4 in the model. While we use nearly all of the 22 current systems (Table 1) we exclude System 10, a faint radial arc without a secure redshift that also lacks bright counterimages. Because even small changes in the mass model produce wildly different predictions for radial systems, the lack of counterimages makes the system fully degenerate with the parameters of the northern cluster halo.

While some systems have only a single MUSE detection (Systems 16, 17, 18, 19 and 22), these objects are often bright in broad-band photometry, and we are able to identify their counterparts in the HFF data directly. In fact, many lens systems with MUSE spectroscopy have at least one counterimage that falls outside of the current footprint, since the GTO data only cover a fraction of the A370 field of view. Though we are unable to confirm these objects spectroscopically, we can identify them with the help of the lens model itself. Specifically, we start with known (spectroscopically confirmed) members of a given lens system and use the model to predict the location of counterimages. From this rough guess, we look for candidates in the HFF data that match the system members (i.e. galaxies with similar colours, morphology and shape), which we take to be the counterimages. We then optimize a new version of the model, including these other constraints. We can compare the models with and without the added constraints, and if the new

Table 1. Multiply imaged systems.

ID[a,b]	RA	Dec	z^c	z range
1.1	39.967 047	−1.576 9172	0.8041	
1.2	39.976 273	−1.576 0558	0.8041	
1.3	39.968 691	−1.576 6113	0.8041	
2.1	39.973 825	−1.584 2290	0.7251	
2.2	39.971 003	−1.585 0422	0.7251	
2.3	39.968 722	−1.584 5058	0.7251	
2.4	39.969 394	−1.584 7328	0.7251	
2.5	39.969 630	−1.584 8508	0.7251	
3.1	39.965 658	−1.566 8560	1.95[d]	
3.2	39.968 526	−1.565 7906	1.95[d]	
3.3	39.977 293	−1.567 2022	1.95[d]	
*3.4	*39.959 758*	*−1.571 3806*	–	
4.1	39.979 704	−1.576 4364	1.2728	
4.2	39.970 688	−1.576 3221	1.2728	
4.3	39.961 971	−1.577 9671	1.2728	
5.1	39.973 473	−1.589 0463	1.2775	
5.2	39.971 110	−1.589 2363	1.2775	
5.3	39.969 472	−1.589 0961	1.2775	
5.4	39.968 580	−1.589 0045	1.2775	
6.1	39.969 405	−1.577 1811	1.0633	
6.2	39.964 334	−1.578 2307	1.0633	
6.3	39.979 641	−1.577 0904	1.0633	
7.1	39.969 788	−1.580 4299	2.7512	
7.2	39.969 882	−1.580 7608	2.7512	
7.3	39.968 815	−1.585 6313	2.7512	
*7.4	39.986 567	−1.577 5688	–	
*7.5	39.961 533	−1.580 0028	–	
*8.1	39.964 485	−1.569 8065	{2.042}	[0.5–5.0]
*8.2	39.961 889	−1.573 6473	{2.042}	
*8.3	*39.984 904*	*−1.570 9139*	–	
9.1	39.962 402	−1.577 8911	1.52 [d]	
9.2	39.969 486	−1.576 2654	1.52 [d]	
9.3	39.982 022	−1.576 5337	1.52 [d]	
*10.1	39.968 585	−1.571 7898	–	
*10.2	39.968 017	−1.570 8820	–	
*11.1	39.963 839	−1.569 3802	{4.667}	[2.5–10.0]
*11.2	39.960 789	−1.574 1702	{4.667}	
*11.3	*39.987 592*	*−1.570 9501*	–	
*12.1	39.969 682	−1.566 6360	{2.858}	[0.5–5.0]
*12.2	39.959 198	−1.575 3221	{2.858}	
*12.3	39.984 100	−1.570 9127	{2.858}	
*13.1	39.979 513	−1.571 7782	{5.119}	[0.5–5.0]
*13.2	39.975 210	−1.568 8203	{5.119}	
*13.3	*39.956 112*	*−1.576 4444*	–	
14.1	39.972 309	−1.578 0910	3.1309	
14.2	39.972 192	−1.580 1027	3.1309	
14.3	39.974 254	−1.585 5770	3.1309	
*14.4	39.981 313	−1.578 2202	–	
*14.5	39.957 673	−1.580 4590	–	
15.1	39.971 328	−1.580 6040	3.7084	
15.2	39.971 935	−1.587 0512	3.7084	
15.3	39.971 027	−1.577 7907	3.7084	
*15.4	39.984 017	−1.578 4514	–	
*15.5	39.958410	−1.579 3722	–	
16.1	39.964 016	−1.588 0782	3.7743	
*16.2	*39.966 037*	*−1.589 0355*	–	
*16.3	39.984 414	−1.584 1111	–	
17.1	39.969 758	−1.588 5333	4.2567	
*17.2	39.985 403	−1.580 8406	–	
*17.3	39.960 235	−1.583 6508	–	
18.1	39.975 830	−1.587 0613	4.4296	
*18.2	39.981476	−1.582 0728	–	
*18.3	39.957 362	−1.582 0861	–	
19.1	39.971 996	−1.587 8654	5.6493	

Table 1 – *continued*

ID[a, b]	RA	Dec	z^c	z range
*19.2	39.985 142	−1.579 0944	–	
*19.3	39.958 316	−1.581 3093	–	
20.1	39.965 279	−1.587 8055	5.7505	
20.2	39.963 619	−1.586 8798	5.7505	
*20.3	*39.986 651*	*−1.581 2606*	–	
21.1	39.966 733	−1.584 6943	1.2567	
21.2	39.967 252	−1.584 9694	1.2567	
*21.3	39.981 539	−1.581 4028	–	
22.1	39.974 406	−1.586 1017	3.1309	
*22.2	39.981 675	−1.579 6852	–	
*22.3	39.957 906	−1.581 0108	–	

Notes. [a]Images labelled with an asterisk (*) fall outside of the MUSE cube and do not have secure redshifts. We identify them in the HFF data, using the A370 mass model as a guide.
[b]Images in italics are predicted by the model, but no suitable counterimage is seen in the *HST* data. We do not include these images as model constraints, but we present them here for completeness. Image 16.2, which is in the MUSE field of view but predicted to fall behind a bright cluster galaxy, is also included here, since it is undetected in MUSE.
[c]Redshifts enclosed in braces ({}) are fit by the model as free parameters. The fit range is given in the 'z range' column.
[d]Redshifts for these systems are taken from Diego et al. (2016).

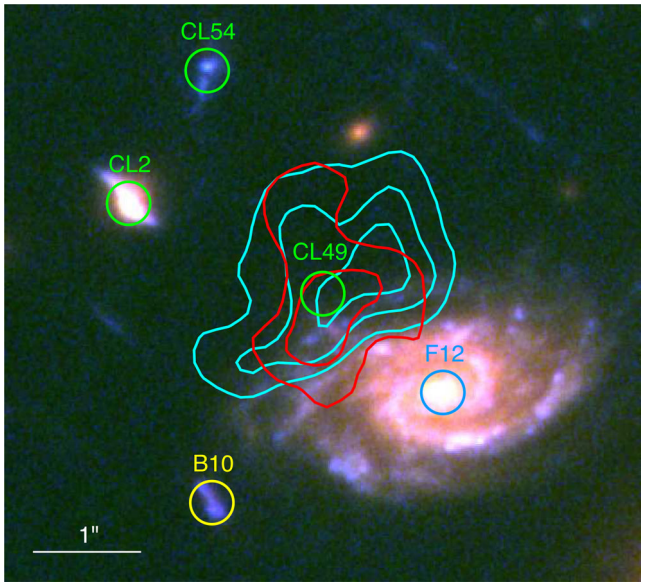

Figure 6. Cluster member CL49, an emission-line object ($z = 0.3843$) not seen in broad-band *HST* imaging. The estimated centroid of the object is shown as a green circle, while the cyan and red contours trace the 1σ, 3σ and 5σ (per pixel) regions of [O II] and H α emission, respectively. Curiously, the long axis of emission seems to have a divergent velocity field, as the flux at either end is slightly redshifted relative to the centre.

results stay within an acceptable error limit: an average model rms displacement of 1 arcsec or lower, we keep the counterimages and start the process again. In this way, we are able to iteratively refine and improve the model until it converges on the best solution.

In the best A370 model, we identify 16 counterimages this way: Images 7.4, 7.5, 14.4, 14.5, 15.4, 15.5, 16.3, 17.2, 17.3, 18.2, 18.3, 19.2, 19.3, 21.3, 22.2 and 22.3. With the exception of the System 7 counterimages, they are all associated with newly identified MUSE objects, again highlighting the power of MUSE as a redshift engine. While the model also predicts the existence of Images 3.4 and 20.3,

Table 2. Cluster members.

ID	RA	Dec	z	m_{F435W}	m_{F606W}	m_{F814W}	Type[a]
Cl1	39.975198	−1.587 9282	0.3582	23.98	22.31	21.55	Ca II H, K
Cl2	39.978460	−1.583 9292	0.3606	24.16	22.96	22.34	H α
Cl3	39.970141	−1.580 7560	0.3609	25.56	24.02	23.18	Ca II H, K
Cl4	39.967945	−1.584 4368	0.3624	24.47	22.56	21.59	Ca II H, K
Cl5	39.970898	−1.584 6121	0.3635	24.52	22.54	21.59	Ca II H, K
Cl6	39.967716	−1.586 6033	0.3639	22.83	20.89	19.86	Ca II H, K
Cl7	39.977458	−1.590 2598	0.3645	24.27	22.71	21.99	Ca II H, K
Cl8	39.974634	−1.583 3866	0.3648	26.09	24.55	23.72	Ca II H, K
Cl9	39.976794	−1.580 8331	0.3649	25.41	23.76	23.00	Ca II H, K
Cl10	39.964373	−1.573 4012	0.3660	23.18	21.25	20.29	Ca II H, K
Cl11	39.964968	−1.575 6005	0.3660	23.42	21.40	20.41	Ca II H, K
Cl12	39.977446	−1.576 4519	0.3680	23.16	21.07	20.02	Ca II H, K
Cl13	39.964290	−1.572 4542	0.3681	23.18	21.25	20.29	Ca II H, K
Cl14	39.975885	−1.575 9172	0.3683	24.37	22.42	21.41	Ca II H, K
Cl15	39.978375	−1.574 3572	0.3683	23.68	21.53	20.49	Ca II H, K
Cl16	39.971815	−1.574 7844	0.3685	23.54	21.84	20.92	Ca II H, K
Cl17	39.971961	−1.584 2487	0.3687	25.34	23.30	22.30	Ca II H, K
Cl18	39.965402	−1.586 0164	0.3701	23.19	21.18	20.15	Ca II H, K
Cl19	39.969599	−1.583 7975	0.3708	22.67	20.66	19.66	H α
Cl20	39.970497	−1.574 8780	0.3708	24.06	22.01	21.01	Ca II H, K
Cl21	39.963783	−1.581 0351	0.3710	21.76	19.82	18.81	Ca II H, K
Cl22	39.971829	−1.586 0732	0.3711	24.65	22.77	21.87	Ca II H, K
Cl23	39.965344	−1.576 0183	0.3716	23.62	21.57	20.54	Ca II H, K
Cl24	39.977262	−1.581 9075	0.3718	23.37	21.18	20.07	Ca II H, K
Cl25	39.972201	−1.580 3644	0.3727	24.83	23.12	22.24	Ca II H, K
Cl26	39.973141	−1.576 8829	0.3728	23.88	21.94	20.95	Ca II H, K
Cl27	39.973889	−1.576 4248	0.3728	25.00	23.21	22.25	Ca II H, K
Cl28	39.973560	−1.574 3250	0.3728	25.05	23.17	22.19	Ca II H, K
Cl29	39.971337	−1.582 2570	0.3731	22.00	19.74	18.66	Ca II H, K
Cl30	39.974778	−1.579 8886	0.3738	25.44	24.60	24.26	H α
Cl31	39.968403	−1.574 6894	0.3742	22.96	20.99	19.95	Ca II H, K
Cl32	39.969132	−1.584 9674	0.3742	23.58	21.57	20.52	Ca II H, K
Cl33	39.971118	−1.586 9043	0.3749	23.13	21.16	20.12	Ca II H, K
Cl34	39.973823	−1.580 8796	0.3753	24.39	22.47	21.51	Ca II H, K
Cl35	39.970597	−1.583 7833	0.3756	23.83	21.72	20.67	Ca II H, K
Cl36	39.972478	−1.584 5667	0.3756	23.01	21.05	20.07	Ca II H, K
Cl37	39.975144	−1.576 8716	0.3762	23.08	21.21	20.25	Ca II H, K
Cl38	39.968075	−1.575 6317	0.3766	23.74	21.77	20.76	Ca II H, K
Cl39	39.972565	−1.583 8926	0.3783	23.01	21.05	20.07	Ca II H, K
Cl40	39.972358	−1.584 3052	0.3784	23.01	21.05	20.07	Ca II H, K
Cl41	39.965603	−1.583 3191	0.3789	25.22	23.43	22.49	Ca II H, K
Cl42	39.967642	−1.573 4009	0.3795	25.21	23.46	22.48	Ca II H, K
Cl43	39.970183	−1.576 3142	0.3798	25.13	23.40	22.46	Ca II H, K
Cl44	39.962843	−1.578 3866	0.3802	24.52	23.60	23.25	H α
Cl45	39.971870	−1.579 7518	0.3807	22.85	21.71	21.07	H α
Cl46	39.975789	−1.585 8086	0.3810	22.52	20.37	19.29	Ca II H, K
Cl47	39.968845	−1.578 0882	0.3826	24.96	22.98	21.98	Ca II H, K
Cl48	39.974799	−1.574 9206	0.3839	25.04	23.02	22.01	Ca II H, K
Cl49	39.977573	−1.584 4846	0.3843	26.76	26.11	25.62	[OII]
Cl50	39.964628	−1.580 2868	0.3844	23.74	21.76	20.73	Ca II H, K
Cl51	39.963103	−1.578 9205	0.3848	25.57	23.82	23.03	Ca II H, K
Cl52	39.969230	−1.577 0399	0.3855	24.12	23.14	22.30	Ca II H, K
Cl53	39.978147	−1.581 4394	0.3873	22.20	20.84	20.12	H α
Cl54	39.978109	−1.583 3172	0.3873	24.16	22.96	22.34	H α
Cl55	39.969088	−1.578 6944	0.3885	22.74	20.54	19.46	Ca II H, K
Cl56	39.973107	−1.575 5088	0.3905	22.91	21.26	20.53	Ca II H, K

Note. [a]Listed emission/absorption lines refer to the most prominent features seen in the galaxy's spectrum.

there are no obvious candidates in the available HFF data, so we do not include them as constraints. The remaining systems (8, 11, 12 and 13) fall outside of the MUSE footprint and lack secure redshift information. Thus, we use the positions of these systems as constraints but leave their redshift values as free parameters to be fit by the model. In some cases, the best-fitting model predicts additional counterimages for these objects (Images 8.3, 11.3 and 13.3), but we again find no obvious counterparts in the HFF data, so we do not use them as model constraints. This is because predicted positions without redshift have significantly larger uncertainties.

Table 3. Other foreground and background objects.

ID	RA	Dec	z	Type
S1	39.972 077	−1.580 5308	0.0000	⋆
S2	39.970 365	−1.585 9742	0.0000	⋆
S3	39.973 933	−1.587 3072	0.0000	⋆
S4	39.964 779	−1.580 1536	0.0000	⋆
F1	39.978 832	−1.575 4827	0.2067	H α
F2	39.975 921	−1.575 0762	0.2070	[O III]
F3	39.978 088	−1.574 6502	0.2181	H α
F4	39.980 006	−1.579 7900	0.2558	H α
F5	39.972 050	−1.574 4911	0.2559	H α
F6	39.965 942	−1.589 3178	0.3050	H α
F7	39.966 252	−1.583 8533	0.3247	H α
F8	39.967 436	−1.587 1793	0.3261	H α
F9	39.978 915	−1.575 0390	0.3263	H α
F10	39.977 545	−1.574 1827	0.3264	H α
F11	39.977 866	−1.577 9488	0.3275	Ca II H, K
F12	39.977 060	−1.584 7684	0.3461	H α
F13	39.972 236	−1.589 3030	0.3465	H α
B1	39.973 514	−1.580 0835	0.4104	[O III]
B2	39.979 117	−1.589 8644	0.4223	[O III]
B3	39.976 931	−1.590 9864	0.4225	[O III]
B4	39.969 400	−1.573 6444	0.4655	Ca II H, K
B5	39.968 908	−1.587 1056	0.5804	[O III]
B6	39.969 464	−1.589 5997	0.6037	[O II]
B7	39.967 551	−1.586 1036	0.6801	[O III]
B8	39.967 227	−1.589 9252	0.8040	[O III]
B9	39.963 801	−1.588 2507	0.8049	[O III]
B10	39.978 094	−1.585 2708	1.0606	[O II]
B11	39.962 676	−1.585 1813	1.0635	[O II]
B12	39.976 042	−1.589 3204	1.3398	[O II]
B13	39.979 281	−1.590 2451	1.4497	[O II]

While we do note that any object without a secure redshift may not be a real counterimage but instead the chance alignment of a different galaxy, the combination of model predictions and visual evidence from the *HST* data makes this scenario extremely unlikely. As a result, we do not consider this possibility in our current lens modelling. However, we will revisit these objects in future work with a larger MUSE mosaic. After adding and removing objects as described above, we are left with 21 unique systems with a total of 66 individual image constraints.

To optimize the model, we feed all parameters and constraints into the LENSTOOL[7] (Kneib et al. 1996; Jullo et al. 2007; Jullo & Kneib 2009) software program, which probes the full parameter space with a Bayesian Markov Chain Monte Carlo (MCMC) sampler. To evaluate a given model, LENSTOOL reconstructs the parametrized mass distribution and transforms the constraint coordinates from the image (observed) plane to the source (undeflected) plane. In the source plane, the program calculates the barycentre of each constraining system, then transforms these results back to the lens plane, creating a set of predicted images that can be compared to observation. By minimizing the rms displacement between prediction and observation, LENSTOOL is thus able to objectively determine the 'best' model for a given set of input parameters (e.g. Kneib et al. 1996; Limousin et al. 2007a).

Following Richard et al. (2014), our initial model includes two massive cluster potentials (each centred on a BCG) and the cluster galaxies selected from the colour–colour cut outlined above. However, after several MCMC iterations with this model, we find that

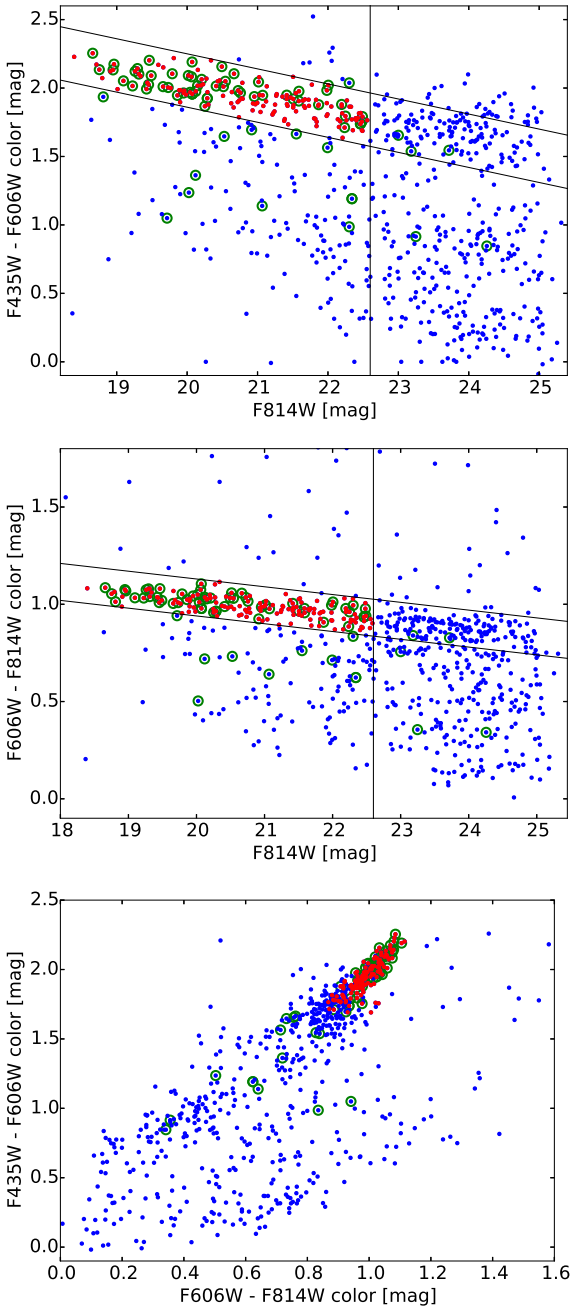

Figure 7. Colour–colour criterion used to select galaxies for mass modelling. Top: objects selected from the ($F435W$–$F606W$) versus $F814W$ colour–magnitude diagram. Diagonal lines trace the 3σ upper- and lower bounds defining the cluster red sequence, while a faint-end magnitude cut-off ($m_{F814W} < 22.6$) is represented by the vertical line. Galaxies selected through this criterion are shown in red. Additionally, spectroscopically confirmed cluster members are highlighted by green rings, and are included in the final model regardless of colour or magnitude. Middle: similar selection diagram, using the ($F606W$–$F814W$) versus $F814W$ colour–magnitude diagram. Bottom: combination of the two colour–magnitude diagrams into a colour–colour diagram. 'Good' objects – those falling simultaneously within both cluster red sequences – are mainly located within a tight locus. The final set of colour–colour selected galaxies are shown in red, while the spectroscopic galaxies are again shown as green rings.

[7] https://projets.lam.fr/projects/lenstool/wiki

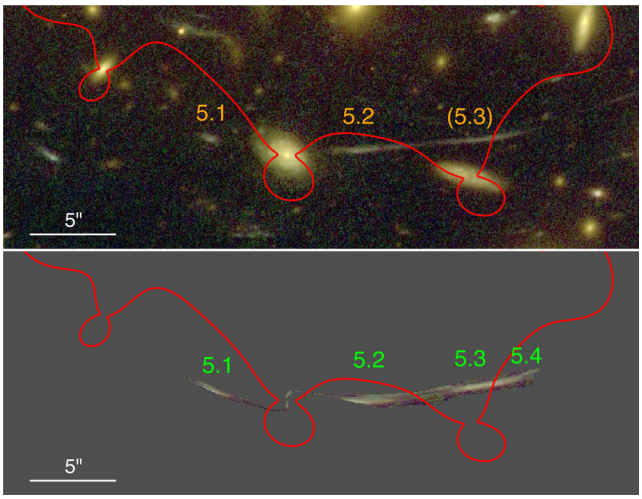

Figure 8. Our new interpretation of System 5. Top: an ACS RGB image of System 5. Bottom: a simulated image, using the lens model. In this simulation, a pixelized image of the galaxy is sent to the source plane and then back to the image plane to be compared with observations. The critical line at $z = 1.2775$ (red line in both panels) is affected by the background $z = 0.6$ spiral galaxy (B6; see Table 3) on the right and crosses the rightmost image previously known as 5.3. We interpret 5.3 as a merging pair of two additional images mirroring only part of the source. This is seen convincingly in the simulation, which reproduce the relative surface brightnesses of the observations well.

no combination of parameter values sufficiently recreates the observed image positions (i.e. with an average rms error <1 arcsec). In particular, we are unable to simultaneously model the positions of the systems in the north and the new MUSE-identified images near the centre. This is most noticeable in System 12, where typical model displacements can be as large as 6 arcsec.

To help correct this disagreement, we first add an elongated, bar-like mass potential (DM3) as a bridge between the two cluster haloes (Table 4). This flattens the mass distribution in the region between the two BCGs, and improves the fit of the central, radial image constraints of Systems 7, 14 and 15. As a consequence of adding the bar, the northern cluster potential (DM2) becomes more elongated and its centroid moves further away from the BCG. This can be explained as a model degeneracy between the positions of DM2 and DM3, since there is a significant overlap between their mass distributions. In fact, the barycentre of the two components falls slightly to the south of the BCG itself.

Even after adding the bar, however, we are only able to reduce the model rms to 1.17 arcsec, with the northern systems still poorly fit. Therefore, we add an additional large-scale cluster potential to the model (DM4), centred near a group of bright galaxies in the northeastern corner of the cluster (see Fig. 9). This location is chosen both because of its proximity to Image 12.3 (the image constraint with the highest rms error), and because it is part of a 'crown' of galaxies sitting above the northern BCG. Since all of the galaxies in the crown are bright and have similar, cluster-like colours and several are spectroscopically confirmed to be cluster members (Mellier et al. 1988) it is possible this collection represents another, unaccounted-for mass component of A370.

As with the other cluster potentials, we allow the dPIE parameters of the crown component to vary freely within a set of priors, though we assume an initial configuration that is more elliptical (like the bar), to better account for the stretched nature of the crown. Including this additional mass clump further improves the fit, reducing the average rms displacement from 1.17 arcsec to 0.94 arcsec, below the benchmark level of rms = 1 arcsec.

To see if even more mass structures are needed to describe A370, we also test a five-clump mass model, placing an additional mass clump on the western side of the A370 crown. Like the eastern clump, we choose locations close to bright cluster galaxies – including the pair of elliptical galaxies near the top of the crown – though we do allow the centroid to vary around these locations. However, this does not significantly improve the fit (rms = 0.88 arcsec) and actually lowers the Bayesian evidence, possibly suggesting an overfit to the data (see Section 5.1). Thus, given the success of the four-clump model in reproducing the image constraint positions, we treat its optimized parameter set as our 'best-fitting' description of the A370 mass distribution. Optimized parameters for all models can be seen in Table 4, and the final model mass reconstruction is shown in Fig. 9.

5 DISCUSSION

5.1 The case for additional mass clumps

While adding two new large-scale mass clumps to the model significantly improves the fit, it is important to ask the question 'Is this additional mass truly necessary?' In other words, are these new mass clumps real features supported by the data, or is it simply a case of overfitting in a sparsely sampled region of the cluster? To answer this, we look at both model and (perhaps more importantly) physical evidence.

From a purely statistical point of view, the Bayesian evidence value ($\mathcal{E}$) can discriminate between models, taking into account and in some cases penalizing additional terms and model complexities, while simultaneously evaluating goodness of fit. Models with larger evidence terms are preferred over those with smaller terms, providing an objective criterion for comparison (see e.g. Limousin et al. 2010). For the A370 models (Table 4), we find that the evidence of the three-clump model ($\log(\mathcal{E}) = -303.19$) is significantly larger than that of the two-clump model ($\log(\mathcal{E}) = -1817.07$), showing that the data strongly prefer a mass distribution that includes a flatter, central 'bar' component. The evidence term of the four-clump model is larger still ($\log(\mathcal{E}) = -201.90$) – though the relative improvement over the three-clump model is not as great – again suggesting a real need for the crown clump. Finally, although the more complex five-clump model has a marginally improved fit over the four-clump model (rms = 0.88 arcsec), its evidence value actually decreases ($\log \mathcal{E} = -202.67$) suggesting that the fifth mass clump is unnecessary and that we are beginning to overfit the system. Additional tests, placing the fifth clump at several other locations throughout the crown, yield similar (or worse) results.

As a complementary check on overfitting, we also calculate the Bayesian information criterion (BIC) term for each model:

$$\mathrm{BIC} = -2 \times \log(\mathcal{L}) + k \times \log(n), \quad (3)$$

where $\mathcal{L}$ is the model likelihood, k is the number of model free parameters and n is the number of model constraints. Lower BIC values are favoured over higher values, and for our models, we again see that the four-clump case (BIC = 455.35) is preferred over all others (we present all values in Table 4), bolstering the claim that the bar and the crown are real, necessary features.

On the physical side of the evidence argument, we first turn to the cluster light distribution. As previously mentioned, the presence of the northern crown of galaxies already suggests an additional mass distribution not captured by the two-clump model. To test this

Table 4. Candidate lens models and best-fitting parameters.

Model name (fit statistics)	Component	$\Delta\alpha^a$ (arcsec)	$\Delta\delta$ [a] (arcsec)	ε^b	θ (deg)	$r_{\rm core}$ (kpc)	$r_{\rm cut}$ (kpc)	σ_0 (km s^{-1})
Two-clump	DM1	$-0.69^{+0.04}_{-0.06}$	$1.83^{+0.32}_{-0.10}$	$0.50^{+0.01}_{-0.01}$	$-73.1^{+0.5}_{-0.3}$	$51.4^{+0.4}_{-1.0}$	[800.0][c]	786^{+2}_{-5}
rms = 2.81 arcsec	DM2	$4.74^{+0.12}_{-0.15}$	$36.64^{+0.11}_{-0.14}$	$0.47^{+0.01}_{-0.01}$	$-104.9^{+0.3}_{-0.3}$	$170.4^{+2.8}_{-1.3}$	[800.0]	1345^{+7}_{-4}
$\chi^2/\nu = 31.97$	BCG1	[−0.01]	[0.02]	[0.30]	[−81.9]	[0.14]	$46.5^{+1.0}_{-1.0}$	205^{+8}_{-2}
$\log(\mathcal{L}) = -1652.47$	BCG2	[5.90]	[37.24]	[0.20]	[−63.9]	[0.14]	$48.3^{+4.2}_{-5.6}$	177^{+34}_{-7}
$\log(\mathcal{E}) = -1817.07$	CL32	[7.92]	[−9.76]	[0.26]	[25.7]	[0.06]	$7.4^{+1.0}_{-1.2}$	90^{+6}_{-1}
BIC = 3404.75	L* galaxy	–	–	–	–	[0.15]	$44.4^{+0.8}_{-2.5}$	163^{+2}_{-2}
Three-clump	DM1	$1.57^{+0.13}_{-0.08}$	$3.05^{+0.01}_{-0.09}$	$0.36^{+0.02}_{-0.03}$	$-78.7^{+1.3}_{-3.3}$	$22.3^{+0.6}_{-1.0}$	[800.0]	564^{+4}_{-3}
rms = 1.17 arcsec	DM2	$19.58^{+1.68}_{-0.50}$	$32.65^{+1.12}_{-2.75}$	$0.90^{+0.03}_{-0.05}$	$-130.6^{+1.1}_{-0.9}$	$149.8^{+6.1}_{-7.5}$	[800.0]	665^{+20}_{-33}
$\chi^2/\nu = 6.00$	DM3	$-3.29^{+0.39}_{-0.35}$	$37.02^{+0.97}_{-0.98}$	$0.54^{+0.02}_{-0.01}$	$91.4^{+1.2}_{-0.8}$	$210.4^{+3.0}_{-4.6}$	[800.0]	1376^{+26}_{-9}
$\log(\mathcal{L}) = -209.75$	BCG1	[−0.01]	[0.02]	[0.30]	[−81.9]	[0.14]	$61.3^{+5.2}_{-2.5}$	177^{+11}_{-5}
$\log(\mathcal{E}) = -303.19$	BCG2	[5.90]	[37.24]	[0.20]	[−63.9]	[0.14]	$63.2^{+1.9}_{-6.4}$	317^{+1}_{-15}
BIC = 554.49	CL32	[7.92]	[−9.76]	[0.26]	[25.7]	[0.06]	$15.3^{+2.5}_{-4.5}$	74^{+3}_{-4}
	L^* Galaxy	–	–	–	–	[0.15]	$45.7^{+2.1}_{-2.3}$	230^{+9}_{-1}
Four-clump	DM1	$1.10^{+0.19}_{-0.17}$	$2.40^{+0.18}_{-0.10}$	$0.22^{+0.03}_{-0.02}$	$-79.3^{+4.6}_{-5.2}$	$20.4^{+0.6}_{-1.0}$	[800.0]	536^{+4}_{-6}
rms = 0.94 arcsec	DM2	$14.04^{+0.73}_{-0.48}$	$30.95^{+0.92}_{-0.81}$	$0.85^{+0.01}_{-0.01}$	$-127.0^{+0.3}_{-0.3}$	$148.4^{+3.9}_{-2.3}$	[800.0]	917^{+10}_{-12}
$\chi^2/\nu = 4.33$	DM3	$-1.11^{+0.28}_{-0.36}$	$31.34^{+1.29}_{-1.03}$	$0.73^{+0.01}_{-0.01}$	$99.2^{+0.5}_{-0.5}$	$179.9^{+5.5}_{-3.7}$	[800.0]	1159^{+9}_{-11}
$\log(\mathcal{L}) = -146.48$	DM4	$-37.58^{+1.15}_{-1.02}$	$42.69^{+1.22}_{-1.20}$	$0.79^{+0.02}_{-0.02}$	$68.2^{+1.5}_{-1.1}$	$55.3^{+6.2}_{-3.1}$	[800.0]	530^{+8}_{-11}
$\log(\mathcal{E}) = -201.90$	BCG1	[−0.01]	[0.02]	[0.30]	[−81.9]	[0.14]	$38.1^{+4.0}_{-3.5}$	185^{+17}_{-6}
BIC = 455.35	BCG2	[5.90]	[37.24]	[0.20]	[−63.9]	[0.14]	$52.4^{+3.9}_{-2.5}$	316^{+12}_{-30}
	CL32	[7.92]	[−9.76]	[0.26]	[25.7]	[0.06]	$28.8^{+6.4}_{-5.2}$	88^{+5}_{-5}
	L^* Galaxy	–	–	–	–	[0.15]	$38.2^{+1.0}_{-2.6}$	197^{+6}_{-8}
Five-clump	DM1	$1.44^{+0.18}_{-0.17}$	$2.35^{+0.33}_{-0.11}$	$0.17^{+0.03}_{-0.03}$	$-73.5^{+6.8}_{-4.3}$	$24.4^{+1.5}_{-1.1}$	[800.0]	561^{+4}_{-3}
rms = 0.88 arcsec	DM2	$9.96^{+0.32}_{-1.19}$	$27.54^{+0.57}_{-1.55}$	$0.83^{+0.02}_{-0.03}$	$-124.3^{+0.8}_{-0.9}$	$129.8^{+4.5}_{-5.2}$	[800.0]	857^{+21}_{-34}
$\chi^2/\nu = 4.29$	DM3	$-2.29^{+0.41}_{-0.88}$	$36.56^{+2.28}_{-0.88}$	$0.76^{+0.02}_{-0.03}$	$100.0^{+0.8}_{-0.8}$	$182.4^{+3.4}_{-8.5}$	[800.0]	1134^{+22}_{-23}
$\log(\mathcal{L}) = -133.64$	DM4	$-38.41^{+1.66}_{-1.24}$	$44.48^{+1.43}_{-1.70}$	$0.80^{+0.02}_{-0.02}$	$73.5^{+4.2}_{-2.3}$	$51.4^{+8.8}_{-4.3}$	[800.0]	531^{+21}_{-18}
$\log(\mathcal{E}) = -202.67$	DM5	$44.27^{+0.11}_{-1.71}$	$53.79^{+8.08}_{-0.28}$	$0.75^{+0.04}_{-0.14}$	$-35.1^{+2.7}_{-5.3}$	$36.9^{+4.5}_{-8.7}$	[800.0]	436^{+52}_{-57}
BIC = 456.27	BCG1	[−0.01]	[0.02]	[0.30]	[−81.9]	[0.14]	$40.6^{+5.3}_{-4.9}$	200^{+11}_{-14}
	BCG2	[5.90]	[37.24]	[0.20]	[−63.9]	[0.14]	$51.0^{+5.0}_{-2.6}$	280^{+17}_{-12}
	CL32	[7.92]	[−9.76]	[0.26]	[25.7]	[0.06]	$5.9^{+4.6}_{-5.7}$	101^{+7}_{-6}
	L^* Galaxy	–	–	–	–	[0.15]	$46.1^{+2.9}_{-1.6}$	199^{+9}_{-10}

Notes. [a] $\Delta\alpha$ and $\Delta\delta$ are measured relative to the reference coordinate point: ($\alpha = 39.971\,34$, $\delta = -1.582\,2597$).
[b] Ellipticity (ε) is defined to be $(a^2 - b^2)/(a^2 + b^2)$, where a and b are the semimajor and semiminor axes of the ellipse.
[c] Quantities in brackets are fixed parameters.

theory, we first isolate the cluster light in the *F*814*W* band (the filter where cluster members are brightest), keeping only the objects selected by the cluster-member colour–colour cut (Section 4) and masking the rest. We then smooth the remaining light with a Gaussian kernel ($\sigma_{\rm smooth} = 10$ arcsec), providing a cleaner view of the light distribution. Comparing this distribution to the four-clump mass model (Fig. 10, left), we find good agreement between the brightest points of the light map and the positions of the large-scale clumps. As expected, the southern cluster halo sits near the southern BCG, the combined northern cluster halo and bar surround the northern BCG, and the fourth clump sits on the eastern side of the crown. Even more promisingly, the orientation of the fourth mass clump is aligned with the distribution of the crown light, even though it is allowed to vary freely in the model. Assuming then that, at least to some degree, the presence of light traces the presence of mass, the agreement between the light map and mass model provides another argument in favour of the four-clump model.

Finally, we also look at the A370 X-ray gas profile, as the presence of hot X-ray gas is often used as a tracer of deep mass potentials. For this, we turn to publicly available, deep *Chandra* data: an 88 ks image of A370, observed using the using the Advanced CCD Imaging Spectrometer S-array (ACIS-S) camera (ID: 08700025, PI: G. Garmire). After smoothing the X-ray map using the ASMOOTH algorithm (Ebeling, White & Rangarajan 2006), we compare the smoothed X-ray map to the positions of the four-clump mass model components (Fig. 10, right). While the results here are not as definitive as in the cluster-light case, we do still see a moderate agreement between the map and the clump positions. Generally, the X-ray contours are also slightly extended in the vicinity of the crown clump, again hinting at the presence of an additional potential well.

Focusing more closely on the X-ray contours, we can see that they follow a distinct box-like pattern, which is especially noticeable in the outskirts of the cluster. Interestingly, the mass contours in the four-clump model have a similar shape, largely driven by the

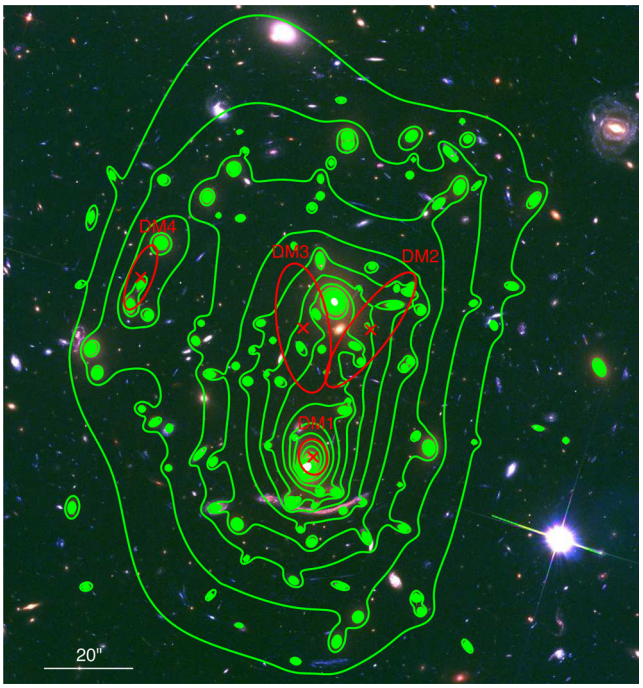

Figure 9. Dark matter surface mass density contours (green) measured from the lens model. Contours are shown in steps of 3×10^8 $M_\odot$ kpc^{-2}, starting from 10^9 $M_\odot$ kpc^{-2}. Highlighted in red are the centroids of the four cluster-scale dark matter haloes. Red ellipses are used to give a rough estimate of the relative shape and strength of each component, but we stress that the actual mass contours are much larger and less elliptical.

overlap between the northern cluster halo and the central bar. Given the rough agreement between the X-ray and mass contours, it is possible that the best-fitting positions of the northern mass clumps are more than a simple degeneracy, but instead driven by physical parameters.

Thus, taken as a whole, the combination of physical and statistical evidence indicates that the additional mass clumps in the cluster centre and crown region are necessary components of the mass model. This suggests an even more complex mass distribution than previously thought, motivating future studies in this area.

5.2 Comparisons with other models

Thanks to the discovery of several new lensing constraints, our picture of the A370 mass distribution is beginning to evolve. While the addition of new mass clumps is the largest change, it is not the only difference. To get a better understanding of these changes and what they mean physically, we can compare our model to previous results. This is especially easy with the models presented by Johnson et al. (2014) and Richard et al. (2014), since they were both also generated with LENSTOOL, using a similar set of parameters. On the whole, while the total mass of A370 remains largely unchanged between models, where the mass enclosed within a 500 kpc circular radius is $\sim 8 \times 10^{14}$ $M_\odot$ in each case, the distribution of mass between various components does not. In particular, we find that the cluster halo associated with the southern BCG (DM1) is much rounder and more compact than either of the previous models, flattening the mass profile in this region. This is predominantly due to the number of radial, five-image systems seen near the southern cluster (Systems 7, 14 and 15), as a more elliptical mass distribution would break

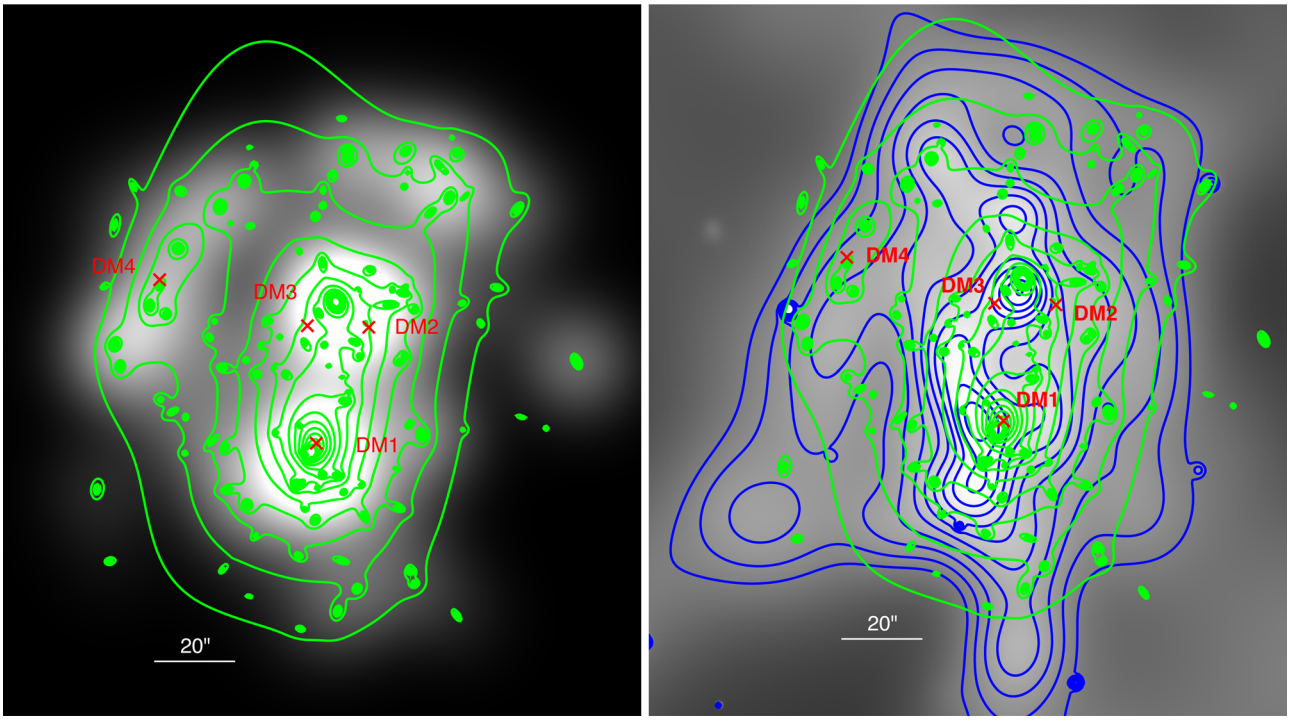

Figure 10. Comparisons between model mass clumps and two physical parameter maps. Left: the smoothed cluster light map. We see an agreement between the mass clump positions and the locations of the brightest cluster light. We also find a good agreement between the orientation of the light in the 'crown' and the fourth mass clump (DM4). Right: the X-ray gas map. We again see an agreement between the map and the large-scale clump positions, along with an agreement in shape and orientation of the X-ray gas contours (blue lines) and model mass contours (green lines). In both cases, the mass contours are the same as those presented in Fig. 9. Taken together these two maps suggest that the bar (DM3) and the crown (DM4) are real features of the cluster, and not a simple case of overfitting the data.

Table 5. Model parameter comparisons.

Parameter	Model[a]	σ_0 (km s^{-1})	ε	θ (degree)	$r_{\rm core}$ (kpc)	$r_{\rm cut}$ (kpc)
DM1	J14	969^{+100}_{-46}	$0.47^{+0.02}_{-0.03}$	$80.8^{+0.99}_{-0.74}$	$88.2^{+8.7}_{-5.7}$	[1500][b]
	R14	833^{+58}_{-6}	$0.59^{+0.04}_{-0.04}$	$-106.0^{+2.8}_{-3.3}$	$64.0^{+8.0}_{-5.0}$	[1000]
	L16	536^{+4}_{-6}	$0.22^{+0.03}_{-0.02}$	$-79.3^{+4.6}_{-5.2}$	$20.4^{+0.6}_{-1.0}$	[800.0]
DM2	J14	1040^{+45}_{-120}	$0.09^{+0.02}_{-0.06}$	$89.4^{+10.0}_{-3.9}$	$94.7^{+3.7}_{-15.0}$	[1500]
	R14	1128^{+37}_{-51}	$0.38^{+0.04}_{-0.05}$	$-89.6^{+2.8}_{-2.4}$	$155.0^{+9.0}_{-12.0}$	[1000]
	L16	917^{+10}_{-12}	$0.85^{+0.01}_{-0.01}$	$-127.0^{+0.3}_{-0.3}$	$148.4^{+3.9}_{-2.3}$	[800.0]
L^* Galaxy	J14	[120]	–	–	[0.15]	[120]
	R14	116^{+16}_{-8}	–	–	[0.15]	$61.0^{+21.0}_{-5.0}$
	L16	197^{+6}_{-8}	–	–	[0.15]	$38.2^{+1.0}_{-2.6}$

Notes. [a]Model Key – J14: Johnson et al. (2014), R14: Richard et al. (2014), L16: this work.
[b]Quantities in brackets are fixed parameters.

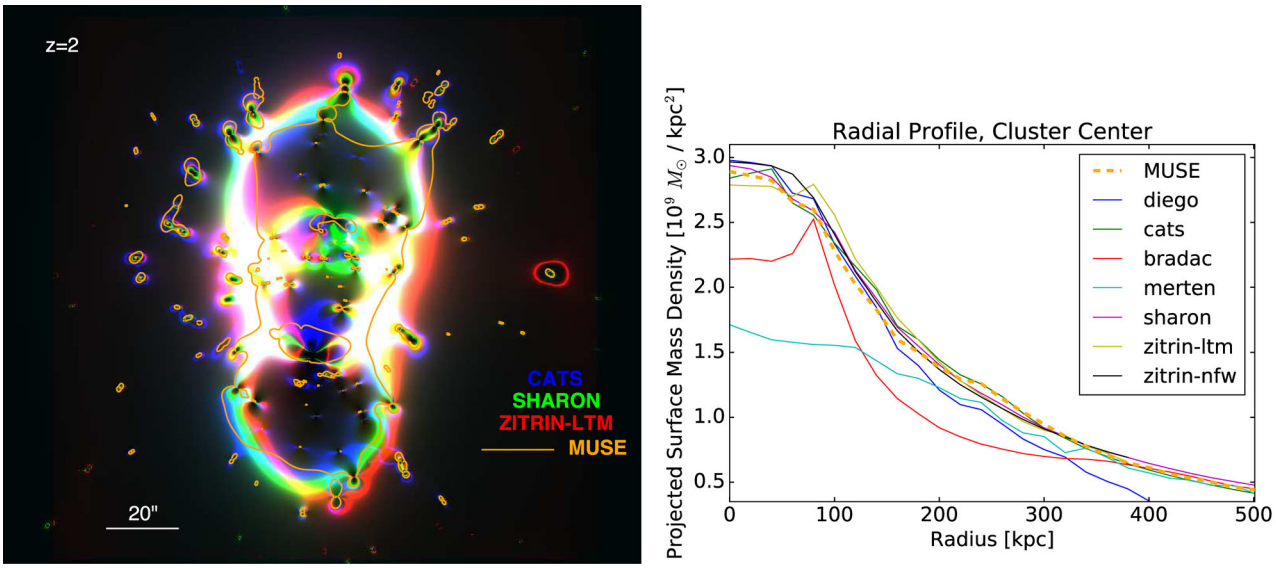

Figure 11. Comparisons between our best-fitting mass model and previous HFF models. Left: magnification maps of the CATS (blue), Sharon (green) and Zitrin-LTM (red) models, compared to the $z = 2$ critical curve of our model (orange line). Areas of high magnification ($\mu > 20$) appear as the coloured regions in each map. We see good agreement between our model and the others, but our model has a larger radial critical region (internal orange line) driven by the discovery of several radial lens systems. Additionally, our critical line has a boxier shape than the other models, due to the orientation of the northern cluster potential and the central bar (Table 4). Right: radial surface mass density profile, using several HFF public models. Our model (orange dashed line) has a lower value at small radii, due to the radial caustic region. At ∼250 kpc, we see a distinct bump, which represents the additional mass clump in the crown.

the symmetry and destroy the radial arcs. Conversely, the northern cluster halo (DM2) is more elliptical and tilted at a steeper angle away from north, though this is largely driven by model degeneracies between DM2 and the central bar component. Both cluster potentials are also considerably less massive in our model, which is another consequence of the bar. Finally, we note that our model favours a significantly larger L^* galaxy velocity dispersion, placing more emphasis on localized substructure contributions to the total mass profile. A list of specific parameter differences can be seen in Table 5.

In addition to specific model parameters, we can also compare the total mass properties of our model. For this exercise, we turn to the public models constructed for the HFF lens modelling initiative. In the left-hand panel of Fig. 11, we show the $z = 2$ critical curve for our best-fitting model, compared to the magnification maps of three different HFF models: 'CATS', from the Clusters As TelescopeS team, (Co-PIs: J.P. Kneib and P. Natarajan), 'Sharon v.2' (PI: K. Sharon) and 'Zitrin-LTM' (PI: A. Zitrin). We select these models because they are constructed using only strong-lensing constraints, and because the resolution of their magnification maps at the core of the cluster is sufficiently high enough to compare their critical curves. In general, the shape of our curve largely traces the high-magnification regions in the other models, suggesting a broad agreement between our work and earlier studies. However, we do note that our curve has a boxier shape, due to the interaction between the northern cluster halo and the central bar and to the presence of the crown clump. Furthermore, the radial critical region (traced out by the internal orange line) is much larger in our model. This is again a result of the rounder, flatter mass distribution predicted by our model, and also highlights the increased area containing radial lensing constraints such as Systems 7, 14 and 15.

These features can also be seen in the right-hand panel of Fig. 11, where we show the radial surface mass density profile for several models (including Diego et al. 2016), starting from a point roughly

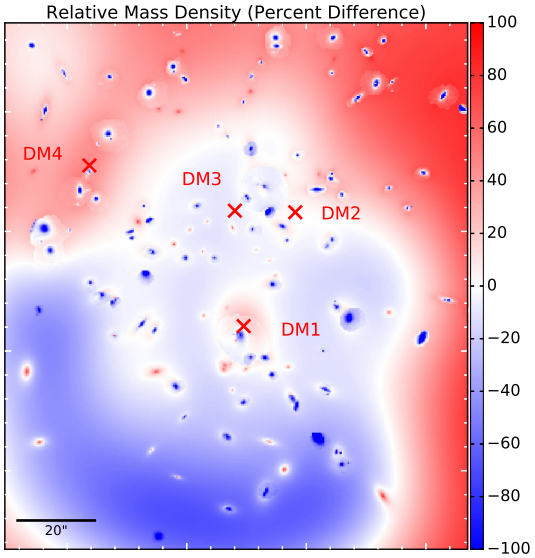

Figure 12. Residual mass density map between our best parametric model and the free-form 'driver' model presented in Diego et al. (2016). In this plot, red represents an overdensity in the parametric model, while blue represents an overdensity in the free-form case. Although there are differences in the spatial distributions of the models, the typical variation is less than 10 per cent. We note that the largest deviations appear in the cluster outskirts, where the absolute mass density is small. As a result, the total mass is roughly the same in both cases.

centred between the two BCGs ($\alpha = 2^{h}39^{m}52\overset{s}{.}937$, $\delta = -1^{\circ}\ 34'\ 37\overset{''}{.}003$). At small radii (<100 kpc), our mass profile is lower than several others, since this region covers the flatter core responsible for the extended radial critical curve. On the other hand, our model profile is slightly higher than the others between 200 and 300 kpc, due to the crown mass clump.

Of course, important spatial information is lost when the mass map is radially averaged, so it is important to look for differences in the full 2D mass distribution, as well. For this test, we compare our four-clump model to the free-form 'driver' model presented in Diego et al. (2016), which is also generated from the HFF data, but constructed in a completely independent way, reducing potential sources of unknown bias. In that work, the driver model is constructed to recreate the positions of 10 very secure lens systems, including seven systems identified here (Systems 1, 2, 3, 4, 6, 7 and 9). Unlike our purely parametric approach, this model uses a broad grid of 2D Gaussians to characterize the smooth, cluster-scale mass distribution, along with a compact light-traces-mass component for bright galaxies (similar to our own method). To make the comparison, we subtract the free-form model's mass density map from our own map, measuring relative differences on a pixel-by-pixel basis. The results can be seen in Fig. 12. Overall, we do see differences between the two approaches: the Diego et al. (2016) model is generally more concentrated and slightly rounder. Our parametric approach shows a noticeable overdensity in the vicinity of the crown, due to the crown mass clump (DM4) in the east, and the extension of the northern cluster clump and the central bar (DM2 and DM3, respectively) in the north-west. The parametric model also has a larger fraction of total mass in the outskirts of the cluster, which is also seen in the radial profile presented in Fig. 11. While model differences can be large at large radii – the parametric model is roughly twice as dense as the free-form model at the edges of the map – we note that the absolute mass density values at these distances are very small ($\sim 10^{8}\ M_{\odot}\ \mathrm{kpc}^{-2}$) and contribute a negligible amount to the total mass budget. Conversely, the relative differences near the cluster centre are typically less than 10 per cent, resulting in an overall good agreement between the two models.

Finally, we can compare our model (and all models) of A370 to other clusters in the HFF programme. The combined rms error for our best-fitting model ($\sigma_i = 0.94$ arcsec) is higher than the error presented in Johnson et al. (2014) ($\sigma_i = 0.82$ arcsec), comparable to the error in Richard et al. (2014) ($\sigma_i = 0.93$ arcsec), and smaller than the error presented in Richard et al. (2010) ($\sigma_i = 1.76$ arcsec). However all of these rms values are larger than the best-fitting models of most other HFF clusters, such as MACS 0416 ($\sigma_i = 0.6$ arcsec; Caminha et al. 2017) or Abell 2744 ($\sigma_i = 0.7$ arcsec; Jauzac et al. 2016). Instead, while not as large, our rms is more similar to MACS 0717 ($\sigma_i = 1.9$ arcsec; Limousin et al. 2016). Like MACS 0717, A370 is a complex cluster, with several interacting mass components covering a large field of view. In fact, the A370 'multiple-image zone' (Fig. 13), the region predicted to contain all multiple images out to high redshift ($z = 10$), is the second largest of all of the Frontier Fields, behind only MACS 0717. Given the similarities, it is therefore unsurprising that the typical rms is also high.

To reduce the total rms further, we need to explore the other areas of the cluster with MUSE. This will help to refine the model even more and allow us to test whether or not our current interpretation is correct. In particular, the crown mass clump may only be a temporary solution; future data may require additional large-scale haloes, or even suggest an alternative to the crown. We cannot be sure of this until we have additional constraints in the north. Fortunately, such a survey is currently underway (PI: F. Bauer), and the results of this study will be the topic of a future paper.

6 CONCLUSIONS

In this paper, we have presented a new mass model for the A370 cluster, taking advantage of deep HFF imaging and new MUSE spectroscopy. Our main conclusions are as follows.

(i) We present a MUSE-based redshift catalogue for A370, consisting of 120 secure redshifts ($\delta z < 0.1$ per cent), including 34 multiply imaged background objects (comprising 15 unique systems), 13 singly imaged background galaxies, 56 cluster members, 13 foreground galaxies and 4 stars.

(ii) Together, HFF and MUSE data are a powerful combination, greatly improving our ability to construct lens models. The MUSE spectroscopy is particularly valuable for this work, as it can be used to blindly identify new lensing constraints without selecting a specific redshift range.

(iii) After constructing a mass model with the new multiply imaged constraints, we find two key differences with previous work.

(1) A central core that is flatter and less massive due to an increase in radial lensing systems.

(2) The need for additional large-scale mass clumps ('the bar' and 'the crown') to better fit lensing constraints in the north of the cluster.

(iv) A lack of model constraints in the north makes accurate comparisons difficult. We will need more MUSE data, covering a larger area of the A370 cluster to discriminate between possible interpretations. These data are currently being taken, and will be the subject of an upcoming paper.

Additionally, our model can be used as a guide for upcoming observations, as high-magnification regions in our models (Fig. 13)

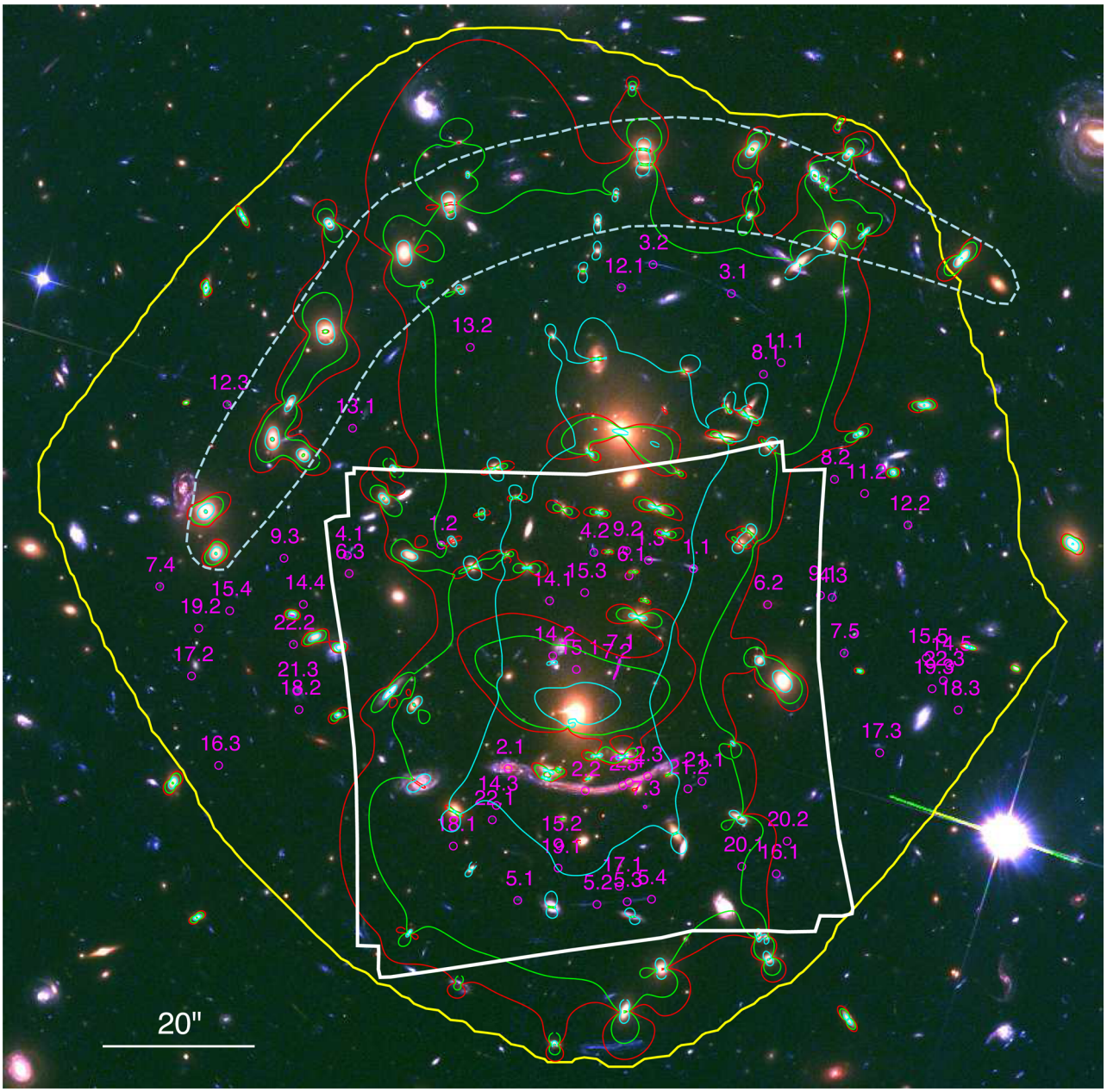

Figure 13. Extent of the 'multi-image zone' (yellow curve) as predicted by the best A370 mass model. This region represents the area that encloses all expected multiple images out to high redshift ($z = 10$). The MUSE data footprint (white square) is again included for reference, and is considerably smaller than the multi-image zone. Additionally, three critical curves are displayed, highlighting lines of high magnification for three redshifts: $z = 1$ (cyan), $z = 3$ (green) and $z = 9$ (red). These lines are heavily clustered around the BCGs and the northern galaxy crown (noted by the dashed contour). Finally, all image constraints used in the model are shown as magenta circles.

should be ideal places to look for new, magnified high-redshift galaxies. With new MUSE spectroscopy on the way, the A370 cluster should continue to provide a wealth of new information in the future.

ACKNOWLEDGEMENTS

The authors wish to thank the anonymous referee for providing several helpful comments and suggestions to improve the manuscript. DJL thanks Jose M. Diego for providing a mass density map of his 'driver' model, which was useful for the quantitative comparisons in Section 5. DJL, JR, BC, GM, VP and JM acknowledge support from the European Research Council (ERC) starting grant 336736-CALENDS. This work has been carried out thanks to the support of the Agence Nationale de la Recherche (ANR) FOGHAR (ANR-13-BS05-0010-02) and the Origines Constituants et EVolution de l'Univers (OCEVU) Labex (ANR-11-LABX-0060). LW acknowledges support by the Competitive Fund of the Leibniz Association through grant SAW-2015-AIP-2. Some of the data presented in this paper were obtained from the Mikulski Archive for Space Telescopes (MAST) at the Space Telescope Science Institute (STScI). STScI is operated by the Association of Universities for Research in Astronomy, Inc., under NASA contract NAS 5-26555.

REFERENCES

Abell G. O., 1958, ApJS, 3, 211
Bacon R. et al., 2010, Proc. SPIE, 7735, 773508
Bacon R. et al., 2015, A&A, 575, A75
Baldry I. K. et al., 2014, MNRAS, 441, 2440
Bernardi M. et al., 2003, AJ, 125, 1849
Bertin E., 2006, in Gabriel C., Arviset C., Ponz D., Solano E., eds, ASP Conf. Ser. Vol. 351, Astronomical Data Analysis Software and Systems XV. Astron. Soc. Pac., San Francisco, p. 112
Bertin E., Arnouts S., 1996, A&AS, 117, 393
Bézecourt J., Kneib J. P., Soucail G., Ebbels T. M. D., 1999a, A&A, 347, 21
Bézecourt J., Soucail G., Ellis R. S., Kneib J.-P., 1999b, A&A, 351, 433
Bina D. et al., 2016, A&A, 590, A14
Bradač M. et al., 2008a, ApJ, 681, 187
Bradač M., Allen S. W., Treu T., Ebeling H., Massey R., Morris R. G., von der Linden A., Applegate D., 2008b, ApJ, 687, 959
Caminha G. B. et al., 2017, A&A, 600, 90
Diego J. M. et al., 2016, MNRAS, preprint (arXiv:1609.04822)
Ebeling H., Edge A. C., Henry J. P., 2001, ApJ, 553, 668
Ebeling H., White D. A., Rangarajan F. V. N., 2006, MNRAS, 368, 65
Ebeling H., Ma C. J., Kneib J.-P., Jullo E., Courtney N. J. D., Barrett E., Edge A. C., Le Borgne J.-F., 2009, MNRAS, 395, 1213
Elíasdóttir Á. et al., 2007, preprint (arXiv:0710.5636)
Ford H. C. et al., 2003, Proc. SPIE, 4854, 81
Fort B., Prieur J. L., Mathez G., Mellier Y., Soucail G., 1988, A&A, 200, L17
Halkola A., Seitz S., Pannella M., 2007, ApJ, 656, 739
Hammer F., 1987, in Bergeron J., Kunth D., Rocca-Volmerange B., Tran Than Van J., eds, Proc. IAP Workshop: High Redshift and Primeval Galaxies. Editions Frontières, France p. 467
Hammer F., 1991, ApJ, 383, 66
Hoag A. et al., 2016, ApJ, 831, 182
Hsu L.-Y., Ebeling H., Richard J., 2013, MNRAS, 429, 833
Jauzac M. et al., 2014, MNRAS, 443, 1549
Jauzac M. et al., 2015, MNRAS, 452, 1437
Jauzac M. et al., 2016, MNRAS, 457, 2029
Johnson T. L., Sharon K., Bayliss M. B., Gladders M. D., Coe D., Ebeling H., 2014, ApJ, 797, 48
Jullo E., Kneib J.-P., 2009, MNRAS, 395, 1319
Jullo E., Kneib J.-P., Limousin M., Elíasdóttir Á., Marshall P. J., Verdugo T., 2007, New J. Phys., 9, 447
Karman W. et al., 2015, A&A, 574, A11
Kawamata R., Oguri M., Ishigaki M., Shimasaku K., Ouchi M., 2016, ApJ, 819, 114
Kimble R. A., MacKenty J. W., O'Connell R. W., Townsend J. A., 2008, Proc. SPIE, 7010, 70101E
Kneib J. P., Mellier Y., Fort B., Mathez G., 1993, A&A, 273, 367
Kneib J.-P., Ellis R. S., Smail I., Couch W. J., Sharples R. M., 1996, ApJ, 471, 643
Limousin M., Kneib J. P., Bardeau S., Natarajan P., Czoske O., Smail I., Ebeling H., Smith G. P., 2007a, A&A, 461, 881
Limousin M. et al., 2007b, ApJ, 668, 643
Limousin M. et al., 2010, A&A, 524, A95
Limousin M. et al., 2016, A&A, 588, A99
Lotz J. M. et al., 2017, ApJ, 837, 97
Lynds R., Petrosian V., 1986, BAAS, 18, 1014
Lynds R., Petrosian V., 1989, ApJ, 336, 1
Massey R. et al., 2015, MNRAS, 449, 3393
Medezinski E., Broadhurst T., Umetsu K., Benítez N., Taylor A., 2011, MNRAS, 414, 1840
Mellier Y., Soucail G., Fort B., Mathez G., 1988, A&A, 199, 13
Mellier Y., Fort B., Soucail G., Mathez G., Cailloux M., 1991, ApJ, 380, 334
Monna A. et al., 2014, MNRAS, 438, 1417
Morandi A., Ettori S., Moscardini L., 2007, MNRAS, 379, 518
Natarajan P., Kneib J.-P., Smail I., Treu T., Ellis R., Moran S., Limousin M., Czoske O., 2009, ApJ, 693, 970
Oguri M., 2010, PASJ, 62, 1017
Paczynski B., 1987, Nature, 325, 572
Patrício V. et al., 2016, MNRAS, 456, 4191
Postman M. et al., 2012, ApJS, 199, 25
Richard J., Kneib J.-P., Limousin M., Edge A., Jullo E., 2010, MNRAS, 402, L44
Richard J. et al., 2014, MNRAS, 444, 268
Richard J. et al., 2015, MNRAS, 446, L16
Rosati P. et al., 2014, The Messenger, 158, 48
Schmidt K. B. et al., 2014, ApJ, 782, L36
Sharon K., Gladders M. D., Rigby J. R., Wuyts E., Koester B. P., Bayliss M. B., Barrientos L. F., 2012, ApJ, 746, 161
Smail I., Dressler A., Kneib J.-P., Ellis R. S., Couch W. J., Sharples R. M., Oemler A., Jr, 1996, ApJ, 469, 508
Soto K. T., Lilly S. J., Bacon R., Richard J., Conseil S., 2016, MNRAS, 458, 3210
Soucail G., Fort B., Mellier Y., Picat J. P., 1987, A&A, 172, L14
Soucail G., Mellier Y., Fort B., Mathez G., Cailloux M., 1988, A&A, 191, L19
Treu T. et al., 2015, ApJ, 812, 114
Umetsu K., Broadhurst T., Zitrin A., Medezinski E., Hsu L.-Y., 2011, ApJ, 729, 127
Weilbacher P. M., Streicher O., Urrutia T., Jarno A., Pécontal-Rousset A., Bacon R., Böhm P., 2012, Proc. SPIE, 8451, 84510B
Weilbacher P. M., Streicher O., Urrutia T., Pécontal-Rousset A., Jarno A., Bacon R., 2014, in Manset N., Forshay P., eds, ASP Conf. Ser. Vol. 485, Astronomical Data Analysis Software and Systems XXIII. Astron. Soc. Pac., San Francisco, p. 451
Zitrin A. et al., 2011, ApJ, 742, 117

This paper has been typeset from a TEX/LATEX file prepared by the author.